Nanoscale

REVIEW

View Article Online
View Journal | View Issue

Cite this: *Nanoscale*, 2021, **13**, 20324

Rational design of metal oxide catalysts for electrocatalytic water splitting

Yiming Xu,†[a] Kaicai Fan,†[a] Yu Zou,[a] Huaiqin Fu,[a] Mengyang Dong,[a] Yuhai Dou,[a] Yun Wang,[a] Shan Chen,[a] Huajie Yin,[a,b] Mohammad Al-Mamun,*[a] Porun Liu*[a] and Huijun Zhao*[a]

Electrocatalytic energy conversion between electricity and chemical bonding energy is realized through redox reactions with multiple charge transfer steps at the electrode–electrolyte interface. The surface atomic structure of the electrode materials, if appropriately designed, will provide an energetically affordable pathway with individual reaction intermediates that not only reduce the thermodynamic energy barrier but also allow an acceptably fast kinetic rate of the overall redox reaction. As one of the most abundant and stable forms, oxides of transitional metals demonstrated promising electrocatalytic activities towards multiple important chemical reactions. In this topical review, we attempt to discuss the possible avenues to construct the electrocatalytic active surface for this important class of materials for two essential chemical reactions for water splitting. A general introduction of the electrochemical water splitting process on the electrocatalyst surface with applied potential will be provided, followed by a discussion on the fundamental charge transfers and the mechanism. As the generally perceived active sites are chemical reaction dependent, we offer a general overview of the possible approaches to construct or create electrocatalytically active sites in the context of surface atomic structure engineering. The review concludes with perspectives that summarize challenges and opportunities in electrocatalysis and how these can be addressed to unlock the electrocatalytic potentials of the metal oxide materials.

Received 24th September 2021,
Accepted 22nd November 2021

DOI: 10.1039/d1nr06285a

rsc.li/nanoscale

[a]*Centre for Catalysis and Clean Energy, School of Environment and Science, Griffith University, Gold Coast Campus, Queensland, 4222, Australia. E-mail: m.al-mamun@griffith.edu.au, p.liu@griffith.edu.au, h.zhao@griffith.edu.au*

[b]*Key Laboratory of Materials Physics, Centre for Environmental and Energy Nanomaterials, Anhui Key Laboratory of Nanomaterials and Nanotechnology, CAS Center for Excellence in Nanoscience Institute of Solid State Physics, HFIPS, Chinese Academy of Sciences, Hefei 230031, P. R. China*

† Equal contributions.

Mohammad Al-Mamun

Dr Mohammad Al-Mamun studied transition metal based electrocatalysts and obtained his PhD degree in materials chemistry in 2016 from Griffith University, Australia. Prior to his PhD, he received research training at Korea National University of Transportation (KNUT) and Shah Jalal University of Science and Technology (SUST). Currently, he is a Research Fellow in Centre for Catalysis and Clean Energy (CCCE), Griffith University. His main research interests include one-step synthesis of earth-abundant functional nanomaterials for electrocatalytic reactions involved in various energy conversion applications.

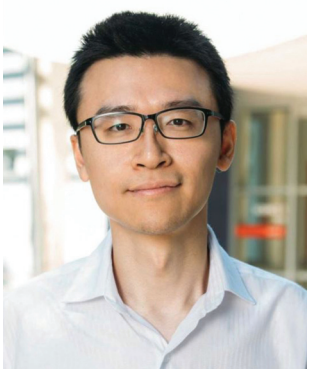

Porun Liu

Dr Porun Liu received his Ph.D. in Chemical Science in 2011 from Griffith University. He subsequently worked as a research fellow in Centre for Catalysis and Clean Energy (CCCE). He was awarded a Griffith University Postdoctoral Research Fellowship in 2015 and an Australian Research Council Discovery Early Career Researcher Award in 2017. He is currently an Associate Professor at School of Environment and Science, focusing on synthesis, in situ *characterizations and electrocatalytic applications of nanostructured catalysts in energy conversion and storage devices.*

1. Introduction

With the increase of global demand for energy, rapid depletion of fossil fuels and intensification of environmental concerns, exploitation of clean and sustainable energy carrier alternatives to fossil fuel with industrial-scale has significantly attracted universal interests.[1,2] Among the various alternatives, hydrogen has emerged as a promising energy carrier to fulfil the increasing energy demand due to its large energy density per unit mass and eco-friendly production possibilities.[1] However, hydrogen does not exist in molecular structures in nature; thus, efficient and sustainable H_2 production, conversion technologies and storage technologies are indispensable for the clean hydrogen cycle. Unlike fossil fuels, hydrogen in molecular or ionic forms needs to be generated for further usage/storage. Currently, large-scale H_2 production involves steam reforming of fossil fuels with CO_2 as a by-product.[1] One promising approach to accomplish clean and sustainable hydrogen production is splitting water molecules into hydrogen and oxygen molecules driven by renewable energy, such as wind power and solar energy.[3,4] However, the practical applications of water electrolysis are partly hindered by the large overpotential and unsatisfactory cost-effectiveness of electrode materials for anodic oxygen evolution reaction (OER) and cathodic hydrogen evolution reaction (HER). Implementation of efficient electrocatalysts is an effective strategy to lower the large HER, OER overpotentials. Ideal water splitting electrocatalysts are featured with high activities with low overpotential to achieve sizeable current density, remarkable robustness and long-term stability. Nowadays, electrocatalysts based on platinum (Pt), ruthenium (Ru) or iridium (Ir) have been the benchmark materials for HER and OER in electrolyzers.[4] However, the scarcity and high cost of these noble metals greatly limit their large scale applications in water electrolysis. Thus, rational design and scalable preparation of highly active and stable noble-metal-free electrocatalysts for efficient hydrogen production have been one of the keys to an industry-scale and rapid deployment of hydrogen technology for sustainable clean energy consumption.

Transition metal oxides are a group of materials abundantly available in Earth's crust. Several features such as mechanical and chemical stability, relatively high charge transfer property even in the amorphous state, and particularly tuneable electronic structure, make metal oxides one of the most promising candidatures for water splitting.[5] Moreover, even though metal phosphides, sulfides, carbides, nitrides are more active materials towards HER, when considering overall water splitting, metal oxides are generally more stable, especially under OER conditions.[6] Also, the fabrication approaches toward metal oxides can be facile and free from harmful chemicals or harsh reaction conditions. Based on these unique properties, metal oxides have been identified as crucial candidates in practical applications, such as thin-film transistors, solar cells, catalysis, energy storage. It is expected that the versatility and functionality of the metal oxides could provide unique opportunities for water splitting. The unexplored potentials of metal oxide as catalysts have inspired and driven many recently published research articles on these fundamentally essential groups of materials as electrocatalysts. Part of the key findings has been summarized in a number of insightful reviews on HER,[7–9] OER[10–14] and overall water splitting.[15–17] A comprehensive review summarizing the active sites, *in situ* characterization techniques, and material engineering strategies for earth-abundant metal oxides for the application of water splitting (HER and OER) has not been published to date. The information provided in the proposed review will allow a timely overview of the useful approaches and also inspirations towards the design of high-performance electrocatalysts for water splitting applications.

In this topical review, we provide an overview of the construction of electrocatalytic active sites (primarily for HER and OER) on metal oxide surfaces. In section 1, we introduce the nature of electrocatalytic active sites in general and their expected features for heterogeneous electrocatalytic water splitting. This is followed by a summary of the characterization techniques for the metal oxides in section 2. The aim of section 3 is to summarize current approaches that could achieve the targeted features of metal oxides. The review is concluded in section 4 with perspectives and outlooks on the future development of high-performance metal oxide electrocatalysts. The review aims to provide colleagues in nanoscience and nanotechnology with a well-established baseline by summarising recent knowledge advance on structure–activity relationship and developments in material engineering strategies for high-performance metal oxide electrocatalysts. We believe the included advancements from theories, characterizations, and strategies surveyed in the review will inspire ideas and innovations in real-world electrolysis. The information included herein has broader implications for the fundamental researches on nanoscale functional

Huijun Zhao

Professor Huijun Zhao is the Director of CCCE at Griffith University, the elected Fellow of the Royal Society of Chemistry (FRSC) and the Royal Australian Chemical Institute (FRACI). He has extensive expertise in energy and environmental nanomaterials, water source control & management, field-based sensing technologies and aquatic environmental quality assessment. One of his current pursuits is to unlock the catalytic powers of nonprecious materials as high-performance catalysts for important catalysis reactions. He has published over 500 refereed journal papers, gained 68 international patents within 8 worldwide patent families and has been a Clarivate Analytics Highly Cited Researcher since 2018.

material, surface chemistry, electrochemistry that extendable to the aforementioned widespread applications of metal oxides.

1.1 Water splitting mechanisms

Nowadays, more than 95% of the global hydrogen is produced by steam reforming natural gas or other fossil fuels.[18] However, the industrial processes produce low purity hydrogen with a large proportion of carbonaceous species such as carbon monoxide. In contrast, water electrolysis is an effective process to produce high-quality hydrogen through the electrochemical conversion of water to hydrogen and oxygen.[19] The electrochemical water splitting provides a clean and sustainable way to convert abundant and renewable water sources into high purity hydrogen.[20] Overall electrochemical water-splitting are composed of two essential reactions, *i.e.*, cathodic HER and anodic OER.

Water splitting occur in two different pathways, in which the reactions are expressed as:

In acidic solution:

$$\text{Cathode}: \ 2H^+ + 2e^- \leftrightarrow \ H_2 \tag{1}$$

$$\text{Anode}: \ H_2O \ \leftrightarrow \ 2H^+ + 1/2O_2 + 2e^- \tag{2}$$

In neutral and alkaline solutions:

$$\text{Cathode}: \ 2H_2O + 2e^- \leftrightarrow \ H_2 + 2OH^- \tag{3}$$

$$\text{Anode}: \ 2OH^- \leftrightarrow \ H_2O + 1/2O_2 + 2e^- \tag{4}$$

The thermodynamic voltage of water splitting is 1.23 V at 25 °C, 1 atm regardless the water media yet it decreases with increase of temperature. In practise, nevertheless, to achieve the electrochemical water splitting, the applied voltages are higher than the thermodynamic potential value. The overpotential (η) is primarily applied to overcome the intrinsic activation barriers on both anode (η_a), cathode (η_c) and some other resistances, *e.g.*, ohmic drop (η_{other}). The practical operational voltage (E_{OP}) for water splitting can be described as:[2]

$$E_{OP} = 1.23 \text{ V} + \eta_a + \eta_c + \eta_{other} \tag{5}$$

η_a and η_b can be optimized by applying highly active oxygen evolution and hydrogen evolution catalysts. η_{other} can be purposely reduced by the rationally designed electrolytic cell. Thus, reduction of the overpotentials will make water splitting reactions more energy-efficient and economically viable.

1.1.1 HER mechanism. HER is a multi-step electrochemical process on the surface of an electrode.[4] The widely accepted reaction mechanisms in acidic and alkaline solutions are either Volmer–Heyrovsky or Volmer–Tafel process:

(1) Electrochemical adsorption (Volmer or discharge reaction)

$$H^+ + M^* + e^- \leftrightarrow \ M\text{–}H^* \text{ (acidic solution)} \tag{6}$$

$$H_2O + M^* + e^- \leftrightarrow \ M\text{–}H^* + OH^- \text{(alkaline solution)} \tag{7}$$

followed by

(2) Electrochemical desorption (Heyrovsky or ion + atom reaction)

$$M\text{–}H^* + H^+ + e^- \leftrightarrow \ M^* + H_2 \text{ (acidic solution)} \tag{8}$$

$$M\text{–}H^* + H_2O + e^- \leftrightarrow \ M^* + OH^- + H_2 \text{ (alkaline solution)} \tag{9}$$

or

(3) Chemical desorption (Tafel or combination reaction)

$$2M\text{–}H^* \ \leftrightarrow \ 2M^* + H_2 \text{ (acid and alkaline solutions)} \tag{10}$$

where M–H* stands for an H atom chemically adsorbed on a single active site of electrode surface (M). The schematic mechanism of hydrogen evolution is depicted in Fig. 1a.[21]

Although the two mechanisms are applicable in both acid and alkaline solutions, it should be noticed that reactants and products are different in various pH values. For example, in acid, only the reduction of a proton into an H* is involved in the Volmer step. While in alkaline solution, besides the creation of the H*, water dissociation is also a critical step for the entire HER process, which requires a breaking of the strong H–O–H covalent bond.

1.1.2 OER mechanism. OER on electrocatalysts consists of four consecutive proton and electron transfer steps. One of the most widely accepted mechanism is the adsorbate evolution mechanism (AEM). This reaction mechanism of OER on a single metal site of metal oxide (M*) can be expressed as:[22]

In acidic solution:

$$H_2O + M^* \ \leftrightarrow \ M\text{–}OH^* + H^+ + e^- \tag{11}$$

$$M\text{–}OH^* \ \leftrightarrow \ M\text{–}O^* + H^+ + e^- \tag{12}$$

$$M\text{–}O^* + H_2O \ \leftrightarrow \ M\text{–}OOH^* + H^+ + e^- \tag{13}$$

$$M\text{–}OOH^* \ \leftrightarrow \ M + O_2 + H^+ + e^- \tag{14}$$

In alkaline solution:

$$OH^- + M^* \ \leftrightarrow \ M\text{–}OH^* + e^- \tag{15}$$

$$M\text{–}OH^* + OH^- \leftrightarrow \ M\text{–}O^* + H_2O + e^- \tag{16}$$

$$M\text{–}O^* + OH^- \leftrightarrow \ M\text{–}OOH^* + e^- \tag{17}$$

$$M\text{–}OOH^* + OH^- \leftrightarrow \ M^* + O_2 + H_2O + e^- \tag{18}$$

The single-site adsorption mechanism of OER is schematically shown in Fig. 1b.[23] It is generally acknowledged that the OER activity of an electrocatalyst depends strongly on the bonding strength of the absorbents on the M active site (M–OH*, M–O* and M–OOH*), of which the adsorption energies are linearly correlated.

Moreover, another OER mechanism (lattice oxygen mediated mechanism, LOM, Fig. 1b) that involves the formation of O–O bonds on adjacent metal ions have also been proven.[23,24] At first, two HO* on the two neighbouring metal ions deprotonate and form two M–O*. Then, the two adjacent O* couple directly with each other, resulting in the formation

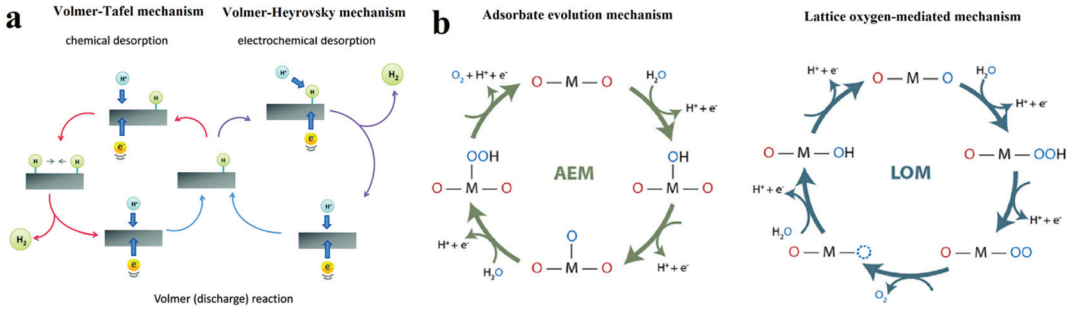

Fig. 1 (a) The schematic of electrocatalytic turn-over of hydrogen evolution on the surface of an electrode.[21] (b) The adsorbate evolution mechanism (AEM) and lattice oxygen mediated mechanism (LOM) of oxygen evolution turnover on the surface of catalyst.[23]

of O–O bond. O_2 is eventually released, and two vacant metal sites are occupied by OH^-. In contrast to AEM, intermediate HOO* is not involved in LOM.

1.2 Kinetics and volcano plots

As the mechanisms shown above, a heterogeneous catalytic reaction consists of a number of coupled reaction steps, *i.e.*, the adsorption of reactant, surface-mediated activation of the adsorbed reactant, and surface-mediated recombination and the eventual desorption of the products from the surface. Based on the Brønsted–Evans–Polanyi relationship, the reaction kinetics of two consecutive dissociative chemisorption steps, the activation energies for each step are estimated to be linear to the dissociative chemisorption energy:[25]

$$E_{a_1} = \alpha_1 \quad \Delta E + \beta_1 \tag{19}$$

$$E_{a_2} = \alpha_2 \quad \Delta E + \beta_2 \tag{20}$$

As the perfectors α_1 is positive and α_2 is negative, one can see the plots of the curves for overall reaction rate (by converting the E_a and reaction rate r with Arrhenius equation) exhibits a Sabatier volcano shape, *i.e.*, with a maximal rate curve at the top of the full solution to the microkinetic model.

Based on the Sabatier principle, for an efficient HER catalyst, its surface ought to allow an interaction strong enough to absorb H* for facilitating the proton–electron-transfer process, while also weak enough to promote the bond breakage and gaseous H_2 release.[26] Nevertheless, it is difficult to establish the quantitative relationship between the energetics of the H* intermediate and the reaction rate. From the perspectives of physical chemistry, the Gibbs free energy change for H* adsorption on a catalyst surface (ΔG_{H^*}) is a widely accepted descriptor for the catalysts. According to the Sabatier principle (a full microkinetic solution for a simple generalized heterogeneous catalytic reaction[25]), if ΔG_{H^*} is zero, the overall reaction has the maximum rate. Furthermore, the relationship between the experimentally measured exchange current density (j_0) and the quantum chemistry-derived ΔG_{H^*} form a volcano curve for a wide range of electrode surfaces.[27] Following this trend, the relationship between the intrinsic electrochemical nature and HER kinetics could be built. Pt-based metals are at the summit of the volcano, as shown in Fig. 2a,[27] which means they have the best activities, and the hydrogen adsorption energy is close to zero. Furthermore, the metals to the left of Pt have strong adsorption to the hydrogen atoms, which blocks the active site and hinders hydrogen generation. While metals to the right of Pt adsorb the hydrogen too weakly, which will not effectively stabilize the intermediate state, thus hindering the occurrence of following hydrogen generation.[25,27]

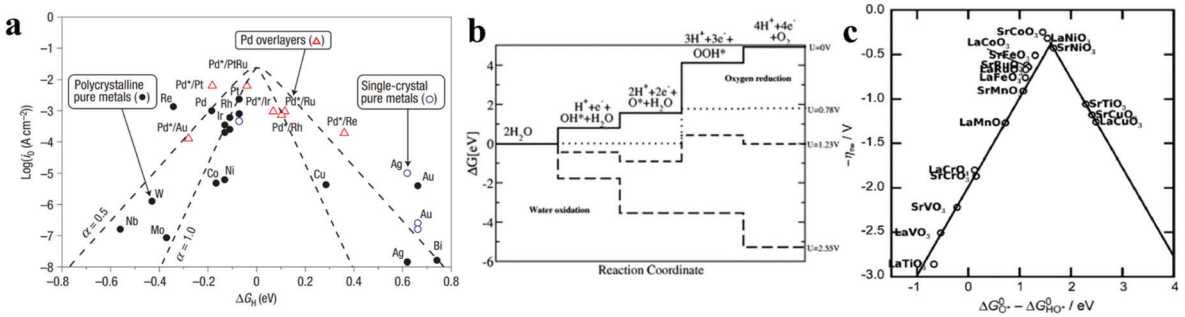

Fig. 2 (a) A volcano plot of experimentally measured exchange current density as a function of the calculated ΔG_H.[27] (b) The free energy diagram for OER steps (from left to right) at different applied potentials (U). Due to the scaling relation between the free energy of the intermediates (OH*, O*, OOH*), they are correlated and thus moved in a concerted manner. At U = 2.55 V, all the OER steps are exothermic (downhill from left to right).[34] (c) Activity trends of the perovskite OER electrocatalysts. The negative theoretical overpotential was plotted against the difference of standard free energy of the ($\Delta G^\circ_{O^*} - \Delta G^\circ_{HO^*}$) step.[22]

Even though the trends in activity for the HER in alkaline media have never been established independently from those results for the HER in acidic media, differences between the descriptors for alkaline and acid HER have been identified. In acid solutions, the reaction is mainly controlled by the hydrogen recombination (the Tafel step), indicating the strong relationship between the activity and the ΔG_{H^*}. However, for HER that occurs in alkaline solutions, the kinetics are determined by the balance between the water dissociation (Volmer step) and the accompanying interaction of the water dissociation product (OH*) on the catalysts.[28–30] In this regard, the optimal ΔG_{H^*} as the sole descriptor is insufficient to describe the HER activity (exchange current in alkaline media is 2–3 orders of magnitude smaller). Thus, other parameters should be further involved and optimized to explore the highly active catalysts. Gong *et al.* suggested that the water adsorption energy and the hydroxide anion adsorption energy can also influence the activity.[31] Low water adsorption decreases the number of reactants, and high hydroxide adsorption energy may result in active site poisoning. Alonso-Vante and coworkers suggested that the kinetics of HER in alkaline is determined by OH adsorption.[32] Thereby, modification of Pt by inducing oxophilic metal centres or sp^2 carbon sites favours the adsorption of OH at low potentials, removes H_{ads} intermediate produced in Volmer step, and thus improves the HER kinetics. Markovic *et al.*, established the relationship overall catalytic activities for HER in alkaline media as a function of $OH–M^{2+\delta}$ bond strength using 3d-M hydro(oxy)oxides and determined that the activity for the established systems follows the order Ni > Co > Fe > Mn.[29] Moreover, Markovic's group identified three parameters based on recent researches, (i) the proton donor, (ii) the energy of formation of the activated complex from proton donor, (iii) the availability of active sites.[33] They believed these parameters could be applied in any aqueous system. These results provided a foundation for the rational design of catalysts for practical HER in alkaline electrolytes.

In contrast, for the AEM of OER, free energy (ΔG) diagrams have been used to investigate the rate-determining steps based on Density-functional theory (DFT) calculations (Fig. 2b).[34] The ΔG values of the intermediates at different steps have a scaling relation and thus change correlatedly.[34] In other words, one free parameter can determine both the free energy diagram and the activity. Later, the scaling relation between the adsorption energies of OOH* and OH* was found to be universal for most of the investigated metal oxide electrocatalysts (Fig. 2c).[22] When the theoretical thermodynamic overpotentials were plotted against the difference of standard free energy of the O* and OH* $\left(\Delta G^{\circ}_{O^*} - \Delta G^{\circ}_{HO^*}\right)$, a volcano relation has been obtained. In line with the Sabatier principle, adsorbate binds to the electrocatalysts on the left branch of the plot too strongly and binds to the counterparts on the right branch too weakly. Also, the $\left(\Delta G^{\circ}_{O^*} - \Delta G^{\circ}_{HO^*}\right)$ values of all the good OER catalysts are constantly about 3.2 eV, compared to the perfect value of 2.46 eV, indicating a minimum overpotential of 0.4–0.2 V. This explains the relatively large overpotential of OER compared to the HER. To tune the $\Delta G^{\circ}_{O^*}$ and $\Delta G^{\circ}_{HO^*}$ values through varying the oxide surface or electrochemical interface may help to improve the OER activities.

On the other hand, in OER pathway following LOM, the intermediate HOO* is not involved (Fig. 1b).[23] Instead, the direct coupling of the lattice oxygen occurs. It is generally believed that oxygen vacancy participation plays an important role in activating the LOM mechanism.[35] Thereby, OER following LOM breaks the scaling relation of HOO* and HO*, and surpassing the maximal activities predicted in the volcano plot in AEM become possible. However, there are still some limitations in the LOM. The process of OER following LOM still involves oxygen intermediates, HO* and O*. Thereby the activity in the LOM is affected by the binding energy between oxygen intermediates and active sites,[36] which means the optimization of adsorption energies of intermediates is important for LOM. For example, Shao-Horn's group performed DFT calculations and galvanostatic oxidation test and proposed that the deprotonation of the surface OH* group was the rate-limiting step.[37] Therefore, a rational-designed OER catalyst following LOM with optimal activities requires both breaking the scaling relation between HOO* and HO* and optimizing the adsorption energies of intermediates.

1.3 Activity descriptors

With the established Sabatier volcano plot and surface scaling relation, one could quantitatively compare the catalytic activity of different surfaces by assessing the bonding strength between the active site and the H adsorbate in HER with DFT calculations. To allow rational design of efficient catalyst, identification of few microscopic surface properties (descriptors) that could link directly with the bonding strength with accuracy is essential. As the d-band model is useful for the understanding of bond formation and prediction of reactivity among transition metals,[38] DFT calculation of the d band centre (relative to the Fermi level) of the transition state has been used as one of the useful descriptors for HER. The higher the d band centre, the more active the metal is (the lower the transition state energy and strong absorption).[39] Also, it is note that other relevant properties such as the filling of the d bands and the width of d bands are strongly coupled and could be used as well. Based on a high-throughput DFT screening scheme, more than 700 binary surface alloys have been assessed theoretically. BiPt has been identified to have high HER activity and this has been experimentally verified.[27]

A number of reaction descriptors have been proposed for the oxygen catalysis (OER and oxygen reduction reaction, ORR), such as the energy of the metal–OH bond (metals),[40] enthalpy of transition from lower oxide to nominal oxide transition ΔH°_{t} (metal oxides),[41] the delocalization and filling (occupancy) of the antibonding σ^* (e_g) states (metal oxides),[42–46] the metal–oxygen covalency (metal oxides),[45,46] $\left(\Delta G^{\circ}_{O^*} - \Delta G^{\circ}_{HO^*}\right)$ (DFT, metal oxides),[34] the number of outer electrons (DFT, metals and oxides).[47] For metal oxide catalyst in solid oxide fuel cell, the descriptor of O p-band centre relative to the Fermi level (DFT)[48] and oxygen and hydroxyl adsorp-

tion energies[22] have been proposed. A statistical machine learning and analysis of the descriptors has done by Shao-Horn *et al.*, who found the number of d electrons, charge-transfer energy and optimality of e_g are important in correlating the OER activity.[49] It should be noted that the utilization of the above descriptors is limited by the structural type of catalysts, and it is vital to find the appropriate descriptor to predict and explain the OER activity. For example, the e_g orbital filling and number of d electrons can be the effective descriptors for perovskite materials, while the e_g occupancy of the cations at octahedral sites can be used for spinel materials.[9,46,50]

These as-mentioned descriptors will always provide the theoretical foundations to improve the electrocatalytic activity towards a specific reaction. Important parameters have been used to describe the performance of an electrocatalyst, such as overpotential (η), Tafel slope, areal activity, mass activity, faradaic efficiency (FE) *etc*.[12] However, when comparing the electrochemical activity, the overpotentials under the same current density are always influenced by the mass loading. Compared with other parameters, turnover frequency (TOF) is the kinetic parameter indicating the intrinsic activity of each active site. TOF is defined as the number of reactant molecules that a catalyst can convert to the desired product per active site in a unit of time. It can be calculated by the equation: $\mathrm{TOF} = (j \times N_A)/(n \times F \times \Gamma)$. j stands for the current density, N_A is the Avogadro number, n is the number of transferred electrons, F is the Faraday constant, and Γ represents the number of active sites. From this equation, it can be deduced that at a given TOF, the more active sites the catalyst own, the larger the current density becomes, representing faster kinetics of the specific reaction. Therefore, it is expected that efficient catalysts possess well-exposed abundant active sites.

These analyses have shown the possibility of fine-tuning of both intrinsic activity and the number of active sites on metal/metal oxides. Thus, in the coming section, we will summarize characterization techniques that have been used for such purposes to allow better constructing the active catalytic sites.

2. *In situ* characterization methods

As exchange current provides useful yet limited information, appropriate characterization methodologies should be involved to study both the electrocatalytic activity and its origin. Two metrics are usually applied to evaluate the electrocatalytic performance of a catalyst. One is the apparent total electrode activity and another is the intrinsic activity of each active site. The relationship between the intrinsic activity and the apparent total electrode activity is vital to the insight of the faradaic charge transfer processes on the electrode surface. Electrochemical approaches, such as voltammetry, electrochemical impedance spectroscopy (EIS) and electrochemical active surface area (ECSA) are widely applied to investigate the relationships and processes towards a specific electrochemical reaction. Other characterizations, including optical spectroscopy and microscopy techniques, are also employed to investigate the composition and structure of electrocatalysts. In addition to these experimental measurements, Density Functional Theory (DFT) calculations are intensively applied to identify the active sites and build the relationship between the structure and the electrochemical activity of the electrocatalysts. Therefore, DFT studies could pave the way in guiding the construction of the electrocatalyst with high activity and stability.

Even though these conventional methods have been proved to be adequate to gain details of the electrocatalyst, it is noteworthy that these details are strongly influenced by environmental conditions, such as atmosphere, temperature, and pressure. Further information is still needed to detect the actual active sites and reaction mechanism towards a specific electrochemical reaction those may guide towards the activity enhancement. Therefore, characterizations at specific voltages are required, and *in situ* experiments are designed for this purpose. Spectroscopic characterizations include Raman spectroscopy, X-ray absorption spectroscopy (XAS), X-ray diffraction (XRD), X-ray photoelectron spectroscopy (XPS), and UV/visible spectroscopy are useful to *in situ* capture the structural transformation of the electrode and oxidation state change of the catalytic species during a specific electrochemical reaction. While microscopic techniques such as atomic force microscope (AFM) and scanning tunnelling microscope (STM) provide direct morphological snap shoot of the evolving electrocatalysts.

The selection of the characterization technique from the tool box is also subject dependent. Currently, material scientists mainly focus on two aspects to improve the performance of electrocatalysts. One aspect is exposing or building more active sites. In this regard, strategies including nanoscale confinement, phase engineering, and facet engineering are utilized. Since some new active phases or facets may form during the electrochemical test, *in situ* Raman spectroscopy, XRD, AFM, and STM are effective tools to detect the newly formed active part and investigate the underlying mechanism. The other aspect is improving the intrinsic activity of each active site. Commonly used methods involve heteroatom doping, defect and strain engineering, *etc*. These methods often result in the changes in electronic structure, such as metal d band and oxygen p band. Therefore, *in situ* XAS, XPS, and UV/visible spectroscopy can be useful techniques to study the properties of metal oxides. The following part illustrates the specific applications of the aforementioned *in situ* techniques.

2.1 *In situ* Raman spectroscopy

Raman spectroscopy is one of the routinely used spectroscopic techniques to observe the vibration, rotation, and other low-frequency modes. Since M–OH, M–OH_2, and M=O vibrations appear in low-frequency range, Raman spectroscopy is a powerful tool to provide information about structure of metal oxides and adsorbates on the surface of metal oxides. This feature endorses it as a useful *in situ* method for the direct investigation of structural changes and intermediates under

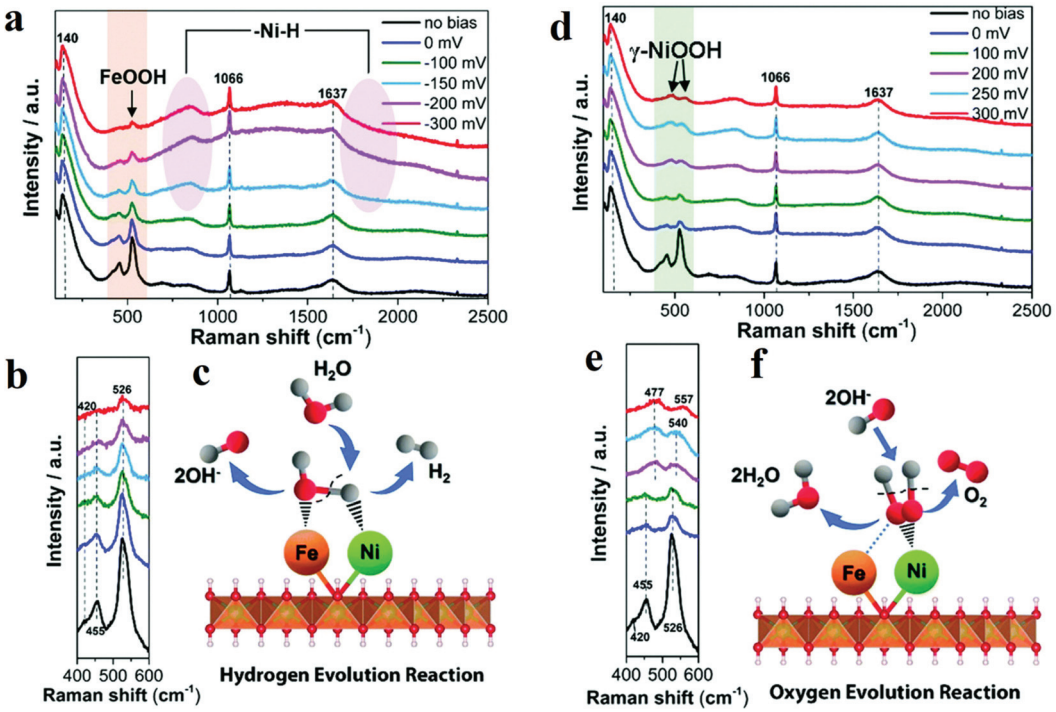

Fig. 3 (a) *In situ* Raman spectra collected in a large wavenumber region from NiFe LDH during HER process in 1 M KOH at various overpotentials *vs.* RHE. (b) Magnification of the corresponding orange wavelength region of (a). (c) Schematic illustration. (d–f) *In situ* Raman spectra of NiFe LDH with 532 nm excitation under OER condition. (d) *In situ* Raman spectra collected in a large wavenumber region from NiFe LDH during OER process in 1 M KOH at various overpotentials *vs.* RHE. (e) Magnification of the corresponding green wavelength region of (d). (f) Schematic picture.[51]

electrochemical reaction conditions. Edvinsson's group synthesized NiFe-layered double hydroxides as the efficient electrocatalyst towards alkaline water splitting.[51] For HER, combining *in situ* Raman spectroscopy data and other *ex situ* characterization results, the author proposed that Ni^{2+} centre adsorbed H_{ad} intermediate (H_{ad}–NiO) and Fe^{3+} centre adsorbed OH_{ad} intermediate (OH_{ad}–FeO) (Fig. 3a–c).[51] A second H_2O would associate with NiO and produce another adsorbed H atom. The two adsorbed H combined to form H_2. The presence of FeOOH facilitated the formation of the second hydrogen with optimal bonding energy and improved the electrocatalytic activity towards HER. For OER, the active phase was identified as γ-NiOOH. The existence of Fe^{3+} introduced high-valent Ni into γ-NiOOH, which was believed to be the reason for the improvement in OER activity (Fig. 3d–f).[51] Wang's group developed Pt–WO_3 as an efficient electrocatalyst towards HER and utilized *in situ* Raman spectroscopy to confirm the real active sites in Pt–WO_3.[52] The characteristic peaks of WO_3 at 268, 710, and 806 cm^{-1} disappeared and reappeared during CV cycles, which proved the phase transition from WO_3 to H_xWO_3. EIS studies further illustrated that the H_xWO_3 phase facilitated fast electron and hydrogen transfer and thus acted as the actual active sites towards HER.

Yeo prepared different OER electrochemical catalysts by depositing Co_3O_4 on various metals and found that substrate metal with larger electronegativity owned better performance towards OER.[53] *In situ* Raman spectroscopy results indicated that at an OER active anodic potential, Co species were oxidized to the valence which was higher than 3 and acted as the active species for OER. By performing the *in situ* surface-enhanced Raman spectroscopy, Smith's group studied the electrocatalytic performance towards OER of two Ni-based catalysts (Ni(Fe)–Bi and Ni(Fe)OOH).[54] The authors concluded from the region *ca.* 900–1150 cm^{-1} that at the potential before the actual OER occurred, some "active" oxygen sites in Ni(Fe)–Bi and Ni(Fe)OOH got negatively charged and acted as OER precursors. Bron's group also investigated Ni and Ni/Fe thin-film electrodes by *in situ* Raman spectroscopy.[55] At OER potentials, the peaks at 475 and 557 cm^{-1} in the Raman spectroscopy results showed the formation of γ-NiOOH. With the increasing Fe contents, the peaks of γ-NiOOH deceased, and I_{475}/I_{557} band ratio also decreased, which meant disorder was introduced into γ-NiOOH. The authors believed that certain amount of Fe can maintain the presence of γ-NiOOH and induce the occurrence of some other structural disorders, which were vital to the improved OER activity. 15% Fe content was determined to be optimum to obtain the best performance.

2.2 *In situ* X-ray absorption spectroscopy

XAS is based on the electronic excitations from the core level to an empty electronic state induced by X-ray photon for the element being investigated. By combining X-ray absorption near edge structure (XANES) and the extended X-ray absorption fine structure (EXAFS), this technique can be used to monitor

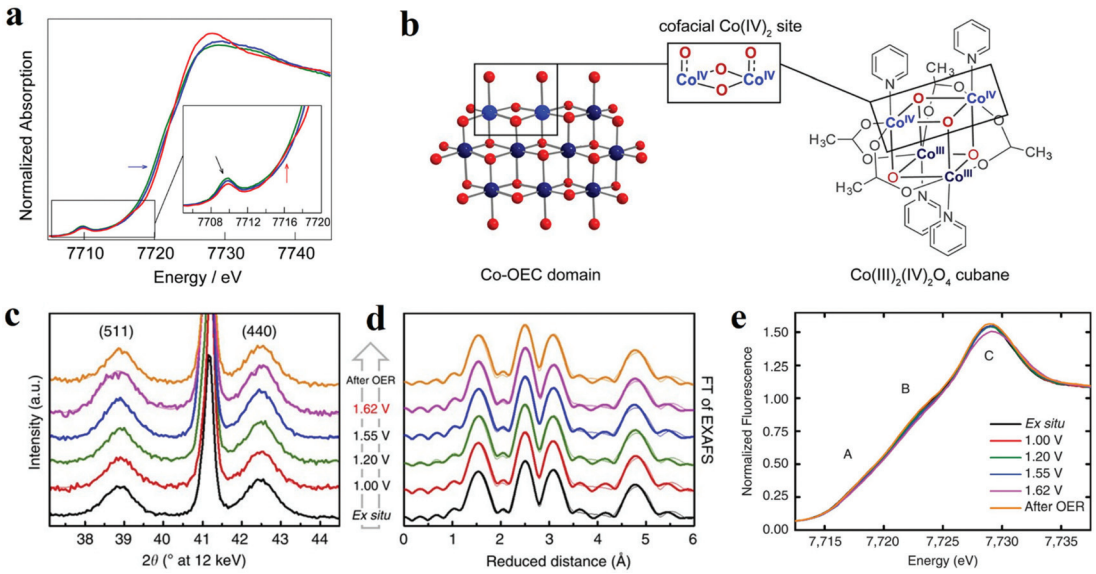

Fig. 4 (a and b) X-ray absorption near edge structure spectra of the three accessible oxidation states of cubane, performed in MeCN + 0.1 M *n*-Bu_4NPF_6.[56] (a) Co K-edge X-ray absorption data for the $Co(III)_4$ (green lines), $Co(III)_3(IV)$ (blue lines), and $Co(III)_2(IV)_2$ (red lines) states, obtained by applying no potential, 0.80, and 1.8 V *vs.* $Fc^{+/0}$, respectively. (b) Co-facial $Co(IV)_2$ sites in Co oxygen-evolving catalyst (Co-OEC) are modelled by a Co_4O_4 cubane. (c–e) *In situ* structural characterization of Co_3O_4 films.[57] (c) *In situ* X-ray diffraction patterns. (d) *In situ* Fourier-transforms (FT) of quasi-*in situ* EXAFS spectra collected at the Co K-edge. (e) *In situ* XANES spectra.

the changes of the electronic structure and the local geometries of the atoms of interest on the catalyst. Herein, it has been applied to study the redox process of metal oxides and identify the active sites during the electrochemical reaction. For the metal oxides, K-edge XAS spectra (with edge positions above 4000 eV) are usually probed, and the ultrahigh vacuum (UHV) condition is not necessary for the "hard" X-ray. Therefore, *in situ* spectrochemical XAS has become a powerful characterization in electrolyte with applied potentials. Brodsky *et al.* prepared oxidic cobalt OER catalysts, and they built the active site as Co_4O_4 cubane.[56] Through electrochemical studies and *in situ* XAS, they found the successive oxidation of $Co(III)_4$ to $Co(III)_2(IV)_2$ (Fig. 4a and b).[56] Combined with DFT calculations, it could be concluded that the antiferromagnetically exchange-coupled Co (IV) sites catalysed OER. Similarly, Bergmann and his group studied the spinel Co_3O_4 as an OER catalyst.[57] The *in situ* cobalt L-edge XAS and *in situ* XRD results showed in Fig. 4c–e indicated that at an OER potential (+1.62 V), the Co species were oxidized to higher valence, which could be proved by the large amount of Co^{3+} and Co^{4+}, and the crystalline phase transformed into an amorphous phase which provided the structure flexibility.[57] The authors believed that the higher valent Co species at the surface, as well as the amorphization, were responsible for catalytic activity. Friebel *et al.* utilized *operando* XAS techniques to observe the changes in the oxidation states and M–O bond lengths of Ni–Fe oxyhydroxides under applied OER potential.[58] The *in situ* EXAFS data suggested that when the Fe contents below 25%, the Fe atoms doped into oxyhydroxide structure and the oxidized catalysts were noted as γ-$Ni_{1-x}Fe_xOOH$. While the Fe levels were above 25%, the Fe atoms tend to nuclear and form γ-FeOOH. Based on the data of changes in oxidation states and M–O bond lengths, DFT results showed that Fe^{3+} cations in Ni–Fe-based oxides lowed the overpotential for OER apparently and were the real active sites for OER.

2.3 *In situ* X-ray diffraction

Another widely used X-ray characterization technique is XRD for investigating the crystal structure of the electrocatalysts. When the incident X-ray beam passes through a crystal, constructive interference and specific diffraction patterns will occur. Different crystalline structures own distinct diffraction patterns. Therefore, *in situ* XRD can offer researchers structure evolution information about crystalline structure, such as crystal phase, crystallinity, lattice parameters (strains), and average grain size, *etc.* during the electrochemical reaction. Combined with *in situ* Raman spectroscopy, it is effective to investigate the active phase changes. Chen's group electrodeposited nanocrystalline cerium dioxide (CeO_2) and amorphous nickel hydroxide ($Ni(OH)_2$) on graphite.[59] For OER, the catalyst showed low overpotential (177 mV@10 mA cm^{-2}) and good durability (over 300 h) at 1000 mA cm^{-2}. The authors compared the *in situ* XRD results of $Ni(OH)_2$ with and without Ce intercalation and they ound intercalation of cerium facilitated the formation of γ-NiOOH exposing (003) facets, which was considered to be the active phase for OER (Fig. 5).[59] As mentioned before, Bergmann investigated the spinel Co_3O_4 at OER potentials.[57] At OER potentials, the crystalline Co_3O_4 structure transformed into amorphous state. While after OER, the amorphous structure returned into the thermodynamically stable spinel crystal. Lattice oxygen was believed to participate OER, leading to the formation of oxygen vacancies. These vacancies ultimately resulted in amorphization.

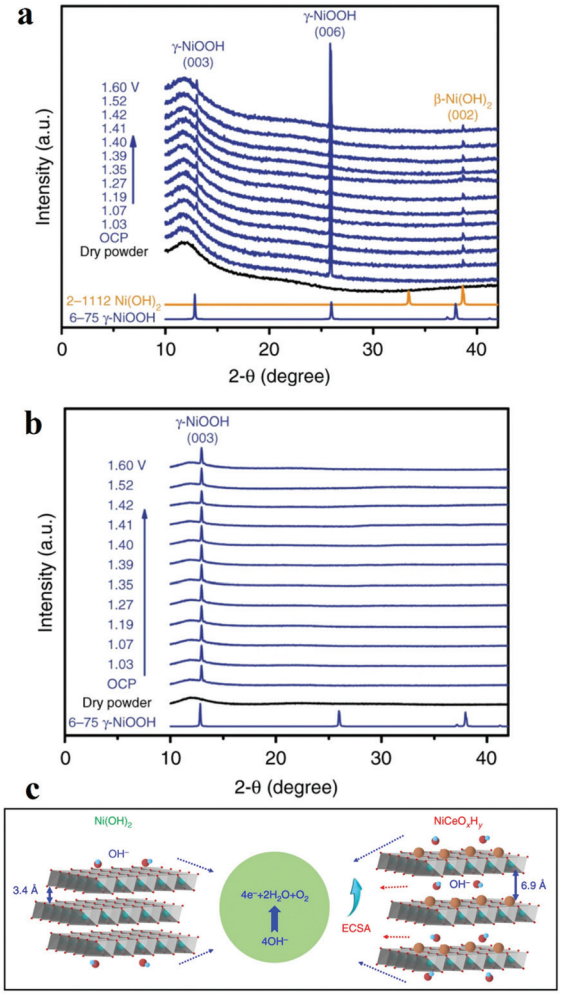

Fig. 5 (a and b) *Operando* XRD patterns collected on (a) $Ni(OH)_2$/NF and (b) $NiCeO_xH_y$ /NF electrodes at different potentials. (c) The OER proceeds more favourably on $NiCeO_xH_y$ with larger interlamellar spacing and higher ECSA relative to $Ni(OH)_2$.[59]

2.4 *In situ* X-ray photoelectron spectroscopy

XPS is a photoemission spectroscopic technique to characterize surface chemistry, bonding structure and composition of surfaces/interfaces by measuring the binding energies of core-level electron generated with soft X-rays based on a photoelectric effect. Since the energy of photoelectron is determined by the energy of the photon and the binding energy of the atomic orbital, one can easily investigate the valence of metal sites and the charge transfer between active sites and coordination atoms. *In situ* XPS therefore enables researchers to obtain bonding information about of different elements in the catalysts under *operando* conditions. Nenning and co-workers employed *in situ* XPS to study $SrTi_{0.7}Fe_{0.3}O_{3-x}$ (STF) thin film.[60] Fe 2p spectra illustrated that at open-circuit voltage, the valence of Fe was between 2 and 3, and the valence band edge was below the Fermi level, resulting in semiconductor-like electronic structure. When cathodic bias was applied, the valence of Fe was reduced to 0. The metallic Fe(0) also extended the orbitals in the valence band towards Fermi level, leading to enhanced HER activity. Friebel's group reported the use of X-ray ambient pressure XPS to investigate a thin Ni–Fe oxyhydroxide film electrodeposited on Au surface as an OER catalyst.[61] When the applied potential increased from 0 to 0.3 V *vs.* Ag/AgCl, the increase of O/OH was detected (Fig. 6a–c),[61]

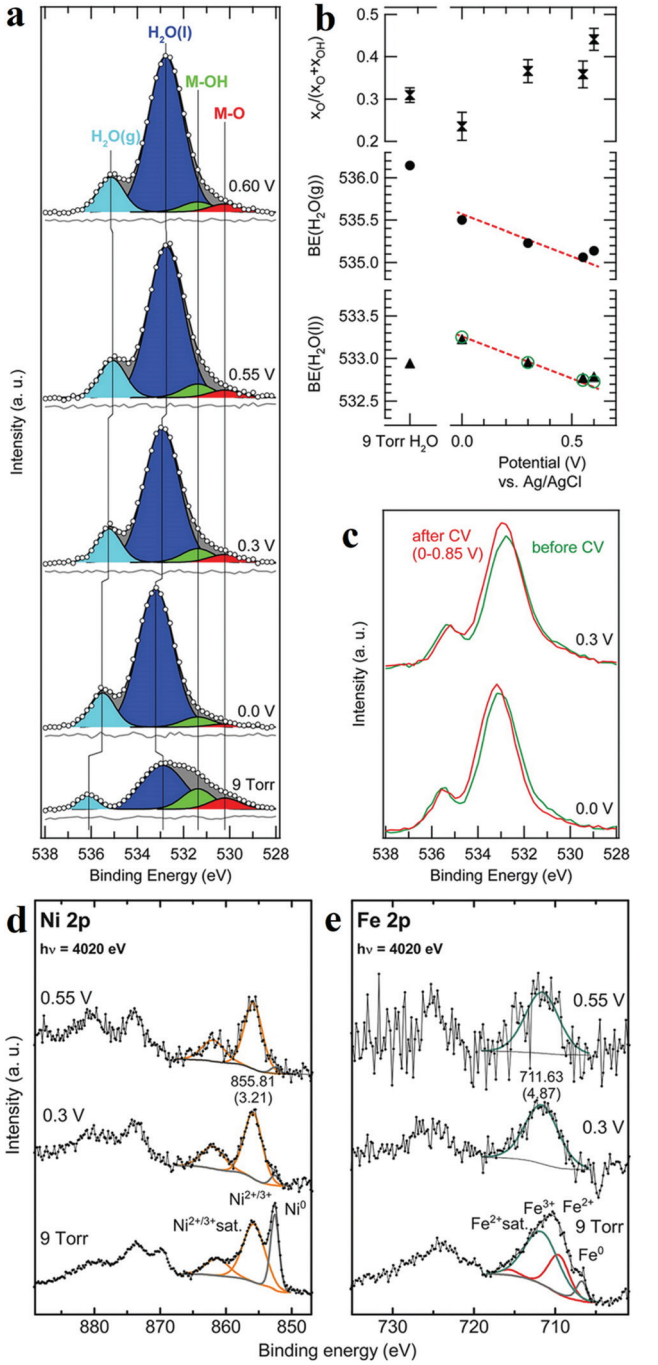

Fig. 6 (a) Normalized and background-subtracted O 1s XPS spectra of Ni–Fe electrocatalyst. (b) Fit results for spectra in (a): relative intensity of the M–O component in the $MO_x(OH)_y$ catalyst, and measured H_2O peak positions (black symbols). (c) Comparison of XPS measurements taken at identical applied potentials before (green) and after (red) the second electrochemical conditioning. Normalized XPS spectra of (d) Ni 2p and (e) Fe 2p transitions for a Ni–Fe electrocatalyst.[61]

which they believed was due to the oxidation of $Ni(OH)_2$ to NiOOH. Combined with Ni and Fe 2p *in situ* XPS spectra (Fig. 6d and e),[61] the authors concluded that oxidation of both Ni and Fe in the film occurred during OER process. Nilsson and co-workers utilized ambient-pressure XPS to *in situ* probe the iridium oxides under OER conditions.[62] The results indicated that under OER conditions, the surface Ir^{4+} was oxidized to Ir^{5+}. This *in situ* observation suggested that Ir^{5+} played an indispensable role in the OER and provided evidence for the OOH-mediated mechanism.

2.5 *In situ* UV/visible spectroscopy

Electron transitions between different energy levels will lead to the absorption of specific wavelengths of ultraviolet or visible (UV/Vis) light. Thereby, one can easily determine the metal redox states by identifying the wavelength of the absorbed UV/Vis light. *In situ* UV/Visible Spectroscopy (UV/Vis) is commonly used to track the change of metal redox states. Görlin *et al.* studied the influence of pH value on the performance of Ni–Fe oxyhydroxide.[63] By using *in situ* UV/vis, they monitored the amount of oxidized Ni^{3+}/Ni^{4+} and found that there was an earlier onset of the redox process with a higher pH value. It was also demonstrated that low-valence Ni was favourable for OER process to occur. Yoshida and co-workers prepared the nickel oxide electrocatalyst by electrodeposition, and they found that during the electrodeposition, the addition of diamines could improve the OER activity of the nickel oxide.[64] *Operando* UV/Vis absorption spectroscopy indicated that 1,2-ethylenediamine combined with Ni^{2+} and formed complexes, which finally facilitated the nickel oxide electrodeposition and increased the number of Ni sites. The improved OER activity mainly derived from the increased number of Ni, which served as active sites.

2.6 *In situ* electrochemical atomic probe microscopy

Integrated with a classical electrochemical cell, Electrochemical Atomic Force Microscopy (EC-AFM) can *in situ* observe the surface morphology or measure the height of catalysts on flat substrates under reaction conditions. Boettcher and co-workers utilized *in situ* EC-AFM to investigate dynamic process of the incorporation of Fe into $Ni(OH)_2$ nanosheets.[65] When applied with high anodic potentials, Fe ions quickly deposited on the top of NiO_xH_y nanosheets and formed FeO_xH_y nanoparticles. While at the open circuit potential, Fe incorporated into and expanded NiO_xH_y, which can be detected by measuring the mean height of the nanosheet. The incorporation of Fe had been further verified by anodic shifts in Ni redox wave. Scanning Tunnelling Microscopy (STM), combined with electrochemical cells, can be employed to *in situ* probe the change of morphology, such as dissolution, degradation, under varying potentials. Moreover, EC-STM can achieve fine measurement of the morphological change with atomic resolution. Paoli *et al.* used EC-STM to observe the dissolution of RuO_2 catalyst under OER potentials directly.[66] The STM images demonstrated that RuO_2 exhibited better stability than deposited Ru, since Ru disappeared from view while RuO_2 showed no corrosion with the same potential scan from 1.3 V to 1.5 V.

2.7 Other techniques determining active sites

Besides the forementioned *in situ* techniques, other electrochemical analyses are also used to determine the concentration of active sites on surface if the current responses are well understood. Since most published work on OER agree that the OER active metal sites undergo *in situ* oxidation and reduction upon voltametric scans. A relatively reliable method is to calculate OER active sites from the redox features of the metal in the CV.[67] The surface concentration of metal sites that participate in OER can be calculated with the integrated area associated with the metal oxidation or reduction (the associated charge) and the number of the transferred electron.

As for determining the concentration of active sites towards HER, since it is difficult to differentiate current associated with the metal redox reactions (if any) superimposed in the cathodic faradaic current, the as-mentioned method is no longer suitable. For the determination of electrochemical active surface area, other electrochemical methods, such as carbon monoxide (CO) stripping, hydrogen underpotential deposition (H-UPD) and peroxide oxidation, have also been used.[68,69] One can also assume that all the metal atoms are active towards HER or OER, and then calculate the active site number and TOF. However, it is noteworthy that this method produced numerous errors.

DFT is often coupled with characterizations to identify the real active sites. After characterizing the geometrical and electronic structure of electrocatalysts, one can build an appropriate model on the basis of the structural information acquired from the characterizations. The essential information such as Gibbs free energy diagram, density of states (DOS), band structure, and charge distribution, *etc*. are accessible with the help of DFT methods.[70–72] These results will finally reflect in descriptors such as d band centre, M–O covalency, and O p-band centre, which regulate the reaction pathways by governing the adsorption energy of intermediates and potential-determining step (PDS). Therefore, the activity of active sites can be predicted with the calculated descriptors and compared with the experimental results.[72] Notably, some electrocatalysts will undergo surface reconstruction and phase transformation, especially when working under OER conditions.[23] Thus it is more accurate to call these catalysts used in the published work "pre-catalysts". The calculation results based on the *ex situ* characterizations without surface reconstruction/activation could be misleading. Thereby, truthful structural information from *in situ* observations under *operando* conditions is more suitable for DFT calculation. Despite some challenges in combinatorial research, such as the lack of DFT tool to effectively simulate the reaction interface under *operando* conditions with affordable computational cost, or the structural complexity at the interface in atomic scale, computation modelling coupled with *in situ* characterizations have been the most effective approach to date and will accelerate exploring high-performance electrocatalysts.

To summarize, *in situ* characterization methods have been briefly summarized as the toolbox for electrocatalyst development that provide researchers with precise information under working conditions as well as guidance to deeper mechanism. The next section of the review is to illustrate that with the help of the characterization techniques, how specific material engineering strategies influence geometric and electronic structures of electrocatalysts and further construct the active catalytic sites on metal oxides.

3. Strategies for activity enhancement

3.1 Nanoscale confinement

Nowadays, the performance of heterogeneous electrocatalysts is still limited by the numbers and intrinsic reactivity of active sites. Moreover, most metal oxides possess limited electronic conductivity and charge transport to the active sites. Compared with the bulk materials, nanostructured materials, such as nanoparticles and nanosheets, typically own higher specific surface areas and thus are endowed with a larger number of surface-active sites. When the diameter of a particulate catalyst is smaller than a specific size (3–5 nm), the significantly reduced coordination number of atoms in outer shells induces dramatic changes in the electronic structure and may improve the catalytic performance. In addition, modulation of the nanostructure, mainly reducing the size of electrocatalysts to the nanoscale, provides an efficient solution to facilitate charge transfer by shortening the charge transport distance. Recently, significant improvements have been achieved by designing the nanostructure of metal oxide catalysts.

The top-down creation of nanoparticles from the parent particles with larger sizes is a common strategy to create a large active area or abundant active sites. Wang *et al.* introduced lithium ions into transition metal oxides and fabricated nanoparticles with an ultrasmall diameter (2–5 nm).[73] It was demonstrated that the ultrasmall $NiFeO_x$ and CoO nanoparticles exhibited superior catalytic activity towards HER and OER compared to nanoparticles with large diameters (~20 nm). Moreover, the obtained catalyst achieved excellent stability of 200 h at 10 mA cm^{-2} without any decay. Different from the catalysts prepared by other traditional chemical synthetic methods,[74] the nanoparticles *in situ* formed *via* this lithium-induced conversion reaction still maintain excellent electrical interconnection while introducing large surface areas and exposed active sites (Fig. 7a–e).[73] From transmission electron microscopy (TEM) images, the interconnected ultrasmall nanoparticles were manifested to have abundant grain boundaries, which acted as the origin of increased surface area and active centres. The rich boundaries were further verified by calculating electrochemical double layer capacities from cyclic voltammetry results. The authors attributed the excellent stability to the *in situ* preparation method involving delithiation reaction process, which endowed excellent mechanical and electrical contacts between the catalyst and the substrate. On the other hand, the coordination environment of atoms in outer shells is significantly affected by the size. The electronic structure is also primarily altered. Zeng *et al.* managed to obtain optimal e_g orbital occupation by controlling the particle size of perovskite $LaCoO_3$.[75] The authors found that when the size was down to 80 nm, $LaCoO_3$ showed the best performance for OER with an overpotential of only 320 mV in 0.1 M KOH electrolyte. The authors explained that the cobalt ions have an optimal electron configuration of e_g ~1.2 according to Shao-Horn' principle[46] when the particle size was ~80 nm which was beneficial to improve the OER activity. By conducting electron energy loss spectroscopy (EELS) spectra, the enhancement stemmed from the spin-state transition from the low-spin state to a high-spin state of cobalt ions at the surface.

Two-dimensional materials, such as nanosheets and thin films, are also widely explored due to their large surface areas, good electrical conductivity, and abundant low-coordinated surface atoms which are essential to accelerate electrochemical kinetics. Sun *et al.* prepared atomically thin cobalt oxide porous sheets and carefully investigated the impact of the nanostructure on OER both theoretically and experimentally.[76] The authors synthesized porous Co_3O_4 ultrathin sheets by heating CoO sheets. TEM and AFM results showed that the porous Co_3O_4 sheets possessed a thickness of only 0.43 nm, which was about half of a unit cell. This ultrathin thickness induced a larger surface area and the expose of all Co^{3+} of Co_3O_4, which was regarded as the active site for OER. More importantly, the coordination number of Co^{3+} atoms decreased from 6 and 5 to 4 or even 3 because of the ultrasmall thickness. According to DFT calculations, the adsorption energy of H_2O molecules on lower coordinated Co^{3+} atoms was larger (0.45 eV), leading to a higher catalytic activity. Furthermore, the density of states at the edge of the valence band and conduction band increased due to the structure disorder on the surface of atomically thick sheets. Therefore, the electron transfer along the conducting channel was promoted, and thus the sluggish OER kinetics was significantly accelerated. Besides, the OER performance for the Co_3O_4 nanosheet was retained even after 10 000 CV cycles, while the bulk counterpart experienced a dramatic drop in OER performance. Through the interfacial charge-transfer resistance test, the outstanding stability was attributed to the unique 2D configuration, which provided intimate contact between the glassy carbon (GC) electrode and the catalyst, and enabled a feasible release of evolved gas bubbles. In another work, ultrathin γ-CoOOH nanosheets were fabricated by atomic-scale phase transformation strategy and manifested superior performance for OER than the state-of-art catalyst.[77] The ultrathin nanosheets were found to be half-metallic, and the electric conductivity was 52 times better than the bulk CoOOH. EXAFS and XPS results in Fig. 7g–i showed that the size confinement led to the existence of surface structural distortion of CoO_{6-x} and rearrangement of Co 3d electrons population.[77] This rearrangement resulted in forming an electron configuration of $t_{2g}^5e_g^{1.2}$, which ultimately improved the electron transfer

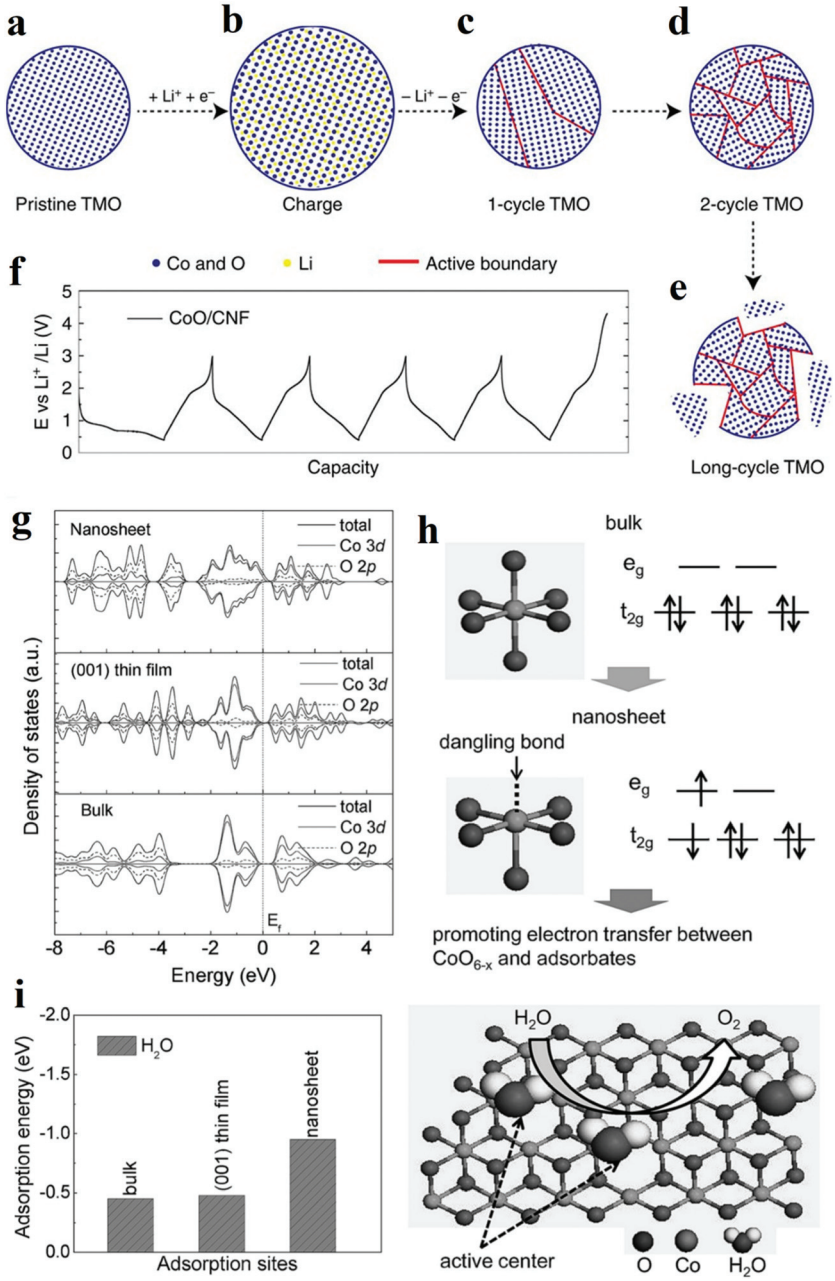

Fig. 7 (a–f) Schematic of transition metal oxides (TMO) morphology evolution under galvanostatic cycles.[73] (a–e) TMO particles gradually change from single crystalline to ultra-small interconnected crystalline NPs. Long-term battery cycling may result in the break-up of the particle. (f) The galvanostatic cycling profile of CoO/CNF galvanostatic cycling. (g–i) The XAS results and theoritical results of γ-CoOOH with different size.[77] (g) Calculated density of states (DOS) for γ-CoOOH nanosheet, γ-CoOOH (001) thin film and bulk γ-CoOOH. (h) Electronic structure transformation of ultrathin γ-CoOOH nanosheet and model of water oxidation on the nanosheet surface. (i) Calculated adsorption energy for ultrathin γ-CoOOH nanosheet, γ-CoOOH (001) thin film and bulk γ-CoOOH.

between surface cations and adsorbed intermediates. The thickness effect of metal oxides on their electrical conductivity was also investigated. Viswanathan *et al.* investigated the relationship between the critical thickness of TiO_2 and the location of valence band maximum relative to the limiting potential for OER to study the charge transport mechanism.[78] With the help of atomic layer deposition (ALD), the authors managed to control the thickness of TiO_2. Through theoretical analysis, it was predicted that the thermodynamic limiting potential for OER was in the band gap of TiO_2, located close to the valence band, and a bias potential was needed to maintain the electrochemical current when the thickness of TiO_2 surpassed a certain value. The experimental results also proved that the overpotential occurred when the thickness exceeded 4 nm.

Since the hierarchical structure provides highly exposed active sites and facilitates the charge and electron transfer of

active species,[79,80] electrocatalysts with different hierarchical structures have been fabricated and presented high electrocatalytic performance. Hierarchical $NiCo_2O_4$ hollow microcuboids with 1D porous nanowires subunits were fabricated by Gao and co-workers.[81] The electrode exhibited excellent activity for overall water splitting, with a small applied potential (1.65 V) to reach a current density of 10 mA cm^{-2} towards overall water splitting as well as excellent stability of 36 h at 20 mA cm^{-2}. Zhu *et al.* prepared a class of novel nickel cobalt oxide hollow nanosponges, which showed excellent catalytic activity towards OER due to their porous and hollow nanostructures.[82]

Overall, the nanoscale confinement strategy, aiming to control the morphology and size of the metal oxide, benefit the electrocatalytic activity by the following four ways. Firstly, the engineering of morphology in nanoscales, such as nanoparticles and nanosheets, often improves the surface specific area and exposes more active sites. Secondly, downsizing into a scale less than a unit cell can dramatically influence the coordination environment of the surface atoms and further impact the intrinsic activity of metal sites. Thirdly, the modulation of size brings a substantial change in the energy band. Then, the modified metal oxides may transform from insulator or semi-conductor to conductor, and the electron transfer pathway is facilitated. Finally, confinement strategies could facilitate more contact between catalysts and substrates and optimize the release of gas bubble, which significantly improve the durability. Thus, nanoscale confinement can be an effective measure to improve catalytic performance.

3.2 Crystal phase and facet engineering

Since most heterogeneous catalysis processes occur on the catalysts' surface, the composition and arrangement of surface atoms are decisive to the activity of catalysts.[83,84] The anisotropic atomic structures such as the coordination environment could be finely tuned by controlled crystal growth. Moreover, distinctive facets and phases usually expose different number of active sites. Therefore, crystal phase and facet can influence the overall activity of electrodes. Accordingly, various surface phase and facet control strategies have been developed to manipulate the catalytic activity and/or create more active sites.

3.2.1 Phase engineering. Crystal phases of metal oxides determine the arrangements of metal and oxygen atoms in the crystal and thus endow the crystal with unique properties. Researchers have made great efforts to investigate the crystal phase-properties relationships. Chen and co-workers prepared three different Ti_2O_3 phase, namely trigonal phase (α-Ti_2O_3), orthorhombic phase (o-Ti_2O_3), and cubic phase (γ-Ti_2O_3) by recrystallization on the substrates at varying temperatures.[85] Among the samples, γ-Ti_2O_3 exhibited the best performance towards HER, reaching a current density of 10 mA cm^{-2} with an overpotential of 271 mV in 0.5 M H_2SO_4. In a typical transition metal oxide (TMO) system, there were two crucial parameters. One was the on-site Coulomb repulsion U, which was the Mott–Hubbard gap inside the 3d band. The other was charge-transfer energy Δ, the energy difference between the oxygen 2p band and transition metal 3d band. Depending on U and Δ, TMOs could be defined into Mott insulators ($U < \Delta$) and charge-transfer insulators ($U > \Delta$) (Fig. 8a).[85] Spectroscopic ellipsometry and light absorption measurements were utilized to determine U and Δ. Fig. 8b also exhibited U and Δ values of α-, o-, and γ-Ti_2O_3, among which γ-Ti_2O_3 owned the largest U and the smallest Δ.[85] Therefore, the electrical conductivity of γ-Ti_2O_3 was the best. Moreover, XAS results showed that γ-Ti_2O_3 owned the most substantial hybridization of O 2p with Ti 3d e_g and t_{2g} orbitals as well as the smallest charge transfer energy, which together led to the delocalization of electrons, and thus increased the conductivity of Ti_2O_3. Through DFT simulation, the stronger Ti–O hybridization resulted in lower d-band centre. The lower d-band centre increased the filling of the antibonding states, weakened the strength of Ti–H bond, and thereby decreased the adsorption energy of H* to optimal value. In another work, Zhou *et al.* prepared a series of manganese oxides with various crystal phases and morphologies through electrodeposition at different pH values, and they found that the valence state of manganese can be changed by controlling the electrolyte composition.[86] Among all the samples, MnO_x with birnessite-like phase and Mn_2O_3 exhibited smaller overpotential for OER in alkaline electrolyte. It was reported that these two phases owned higher surface concentrations of Mn(III), which acted as the active sites for OER in MnO_x. Along with porous structures, these phases finally rationalized superior activities for OER. Su *et al.* combined both DFT calculation and electrochemical methods to identify active surface phases in MnO_x for ORR and OER.[87] Electrochemical test results showed that the α-Mn_2O_3 was a promising bi-functional catalyst for both ORR and OER, with the onset potentials of 0.83 V and 1.5 V, respectively. Through theoretical calculation, the authors predicted that the surface phase of MnO_x changed with pH and applied electrochemical potential, which was also accurately verified by the XRD experiments. Based on the results, the authors found that different surface phases owned different coordinated oxygen atom numbers to Mn, which affected the binding energy of intermediates significantly. For example, if the coordinated oxygen atom number on Mn_2O_3 changed marginally, the $\Delta G_{O^*} - \Delta G_{OH^*}$ would change by 0.7 eV. Varying the surface phase can also change the difference between HOO* free energy and HO* free energy, decreasing from 3.2 eV to a lower value, and the OER electrocatalytic activity was enhanced. *In situ* phase engineering is also effective in improve spinel and perovskite materials' performance. Tung *et al.* prepared a single-crystal Co_3O_4 nanocube to underlay with a thin CoO layer as an efficient OER catalyst.[88] *In situ* XRD demonstrated that the surface CoO layer *in situ* transformed into active oxyhydroxide phase and acted as the active skin for OER. Notably, the CoO film also protected Co_3O_4 single-crystal nanocubes under OER conditions, avoiding volume expansion/contraction which may harm the scaffold Co_3O_4. As a result, the as-prepared catalyst exhibited excellent stability of more than 1000 h. Lee and co-workers prepared a hexagonal perovskite, $BaNiO_3$, exhibiting better activity and stability for OER than IrO_2 catalyst.[89] The

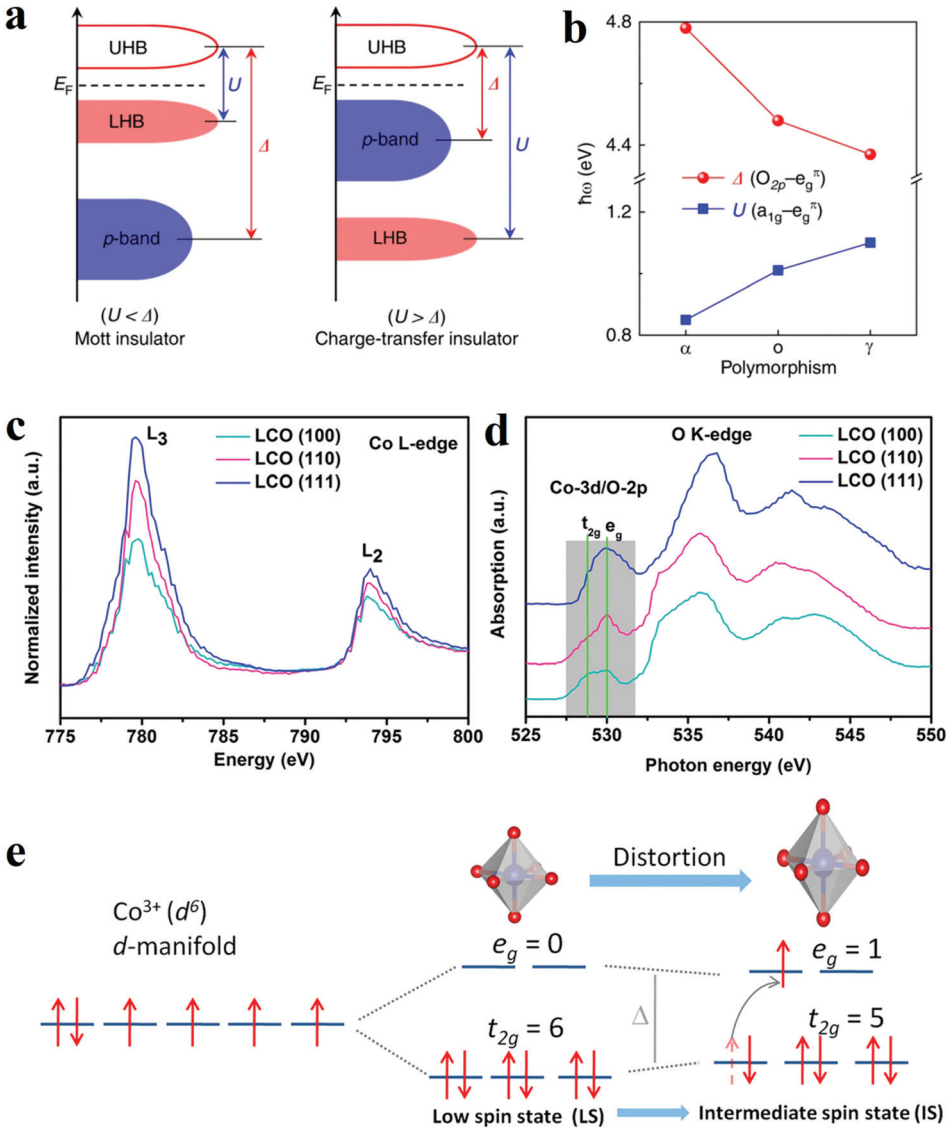

Fig. 8 (a and b) The influence of phase engineering on the energy band of Ti_2O_3 polymorphs.[85] (a) Schematic energy band diagram for the Mott insulator and charge-transfer insulator. (b) Evolution of the U and Δ in Ti_2O_3 polymorphs. (c–e) XANES spectra and schematic illustration of intermediate spin state transition.[93] (c and d) Co L-edge (c) and O K-edge (d) XANES spectra for LCO (100), (110), and (111) films. (e) Schematic illustration of the transition of electrons from t_{2g} to e_g orbital and the evolution of intermediate spin state.

authors found that the superior activity derived from the phase transformation from $BaNiO_3$ to $BaNi_{0.83}O_{2.5}$ during OER by conducting DFT calculations. The phase transformation brought two main changes. First, compared to $BaNiO_3$ with e_g occupancy near zero, $BaNi_{0.83}O_{2.5}$ owned e_g occupancy near unity, which was better for OER according to the principle proposed by Shao-Horn.[46] On the other hand, the phase engineering also influenced Ni oxidation state and coordination environment, switching Ni^{4+} in first shell coordination into Ni^{2+} in distorted-prism (P) coordination, which was proved to be more active for OER.

3.2.2 Facet engineering. In addition to phase engineering, facet engineering is another effective tool to design ideal electrocatalysts. The key towards the facet control is to induce anisotropic crystal growth. Fang *et al.* synthesized a series of $NiCo_2O_4$ exposing different crystal facets towards efficient overall water splitting under alkaline conditions through a traditional hydrothermal method.[90] Experimental results indicated that the nanosheet exposing (110) planes obtained a better electrochemical activity for overall water splitting than octahedron exposing (111) planes and truncated octahedron exposing (111) and (100) planes. DFT calculations indicated that the specific coordination environment of metal sites in (110) planes brought highest surface energy, smallest free energy ΔG_{H^*} for HER and lowest theoretical overpotential value for OER. Therefore, (110) crystal planes exhibited a superior electrochemical catalytic activity for overall water splitting. Han *et al.* designed a series of surface-tailored Co_3O_4

nanoparticles on N-doped reduced graphene oxide by the conventional hydrothermal method.[91] The authors investigated their performance for oxygen reduction and evolution reactions (ORR/OER) and metal–air batteries. Electrochemical results suggested that the nanocomposite with Co_3O_4 nanopolyhedron (NP) exposing (112) crystal planes (Co_3O_4-NP/N-rGO) had superior bifunctional electroactivity for ORR/OER over other counterparts with exposing (001) crystal planes and with (001) + (111) crystal planes. There were two species of cobalt ions, the tetrahedrally coordinated Co^{2+} ($Co^{2+}{}_{Td}$) and octahedrally coordinated Co^{3+} ($Co^{3+}{}_{Oh}$). Through DFT calculations, it was demonstrated that facets with more $Co^{3+}{}_{Oh}$ species could obtain the appropriate extent of O═O elongation and optimize the adsorption, dissociation and desorption of oxygen species. Hence, the Co_3O_4-NP/N-rGO exposing (112) facets with more abundant $Co^{3+}{}_{Oh}$ sites presented better catalytic performance than the counterparts with other exposing crystal facets. Wu *et al.* also compared the OER electrocatalytic activities of α-Fe_2O_3 nanocrystals exposing different facets, namely (012)-O, (012), (104) and (110).[92] The hematite exposing (012)-O and (012) showed advantageous catalytic activity for OER, with a lower overpotential of 305 mV and 317 mV at 10 mA cm^{-2}. Theoretical results through DFT calculations indicated the (012) facet owned the active sites with the highest activity since they possessed a relatively low free energy for all intermediates from OER. As a result, the process of adsorption/desorption was optimized, and the kinetics barrier became lower. The facet engineering have also been used to improve perovskite materials. Wu and co-workers optimized the OER performance of $LaCoO_3$ through spin-state regulation by controlling facet orientation.[93] Three different facet orientations, basically (111), (110), and (100), brought a varied degree of distortion of CoO_6 octahedron, which corresponded to the transformation of the spin state from the low spin state ($t_{2g}{}^6e_g{}^0$) to the intermediate spin state ($t_{2g}{}^5e_g{}^1$) (Fig. 8e).[93] The change in spin state was confirmed by XANES spectra (Fig. 8c and d).[93] Benefit from the intermediate spin state, the film with (100) orientation obtained optimal conductivity, e_g electron filling states (0.87), as well as adsorption free energy of O species. These characters collectively resulted in an outstanding performance for OER with an overpotential of 470 mV at 10 mA cm^{-2}.

To sum up briefly, surface atomic arrangements of a bulk crystal are readily controllable with crystal phase and facet engineering. This provides scientists with an essential "knob" to fine tune the electronic structure and electrocatalytic nature even with the similar elemental composition. Firstly, engineering of phase and facet endow changes in energy band of metal oxides, which might change insulating characteristics into half-metallic or metallic one and modulate electronic transportation. Secondly, the engineering in phase and facet often changes the coordination environment of metal site and the M–O electronic structure, and thereby modulates the intrinsic activity, especially for OER. Finally, even assuming that active sites are with equal activity, crystalline catalysts with specific phases and facets expose more active sites, which certainly improve the overall electrochemical performance.

3.3 Heterostructure

It is scarce that overall water splitting in practice undergo electrochemical turnover on electrocatalysts with high homogeneity. Recently, construction of heterostructure or creation of interfaces with the remarkable synergistic effect has become a focused research topic. According to the experimental and theoretical studies, the strong coupling interactions and interface reconstruction between composites can not only promote electrochemical reaction activity but also expose more active sites. The strategy of fabricating the rationally designed heterostructures can be adopted to prepare catalysts with excellent performance.

It has been proven that HER in alkaline solution significantly depends on activating and cleaving O–H bonds of water molecules and facilitating the adsorption and desorption of the formed H atoms. In this regard, the novel concept of composite materials facilitating these two key aspects of HER process in alkaline solution has been reported. A typical example is a heterostructure composed of oxide and metal, in which the oxide acts as the active site for the dissociation of water, while the metal facilitates the adsorption and desorption of hydrogen atoms. Subbaraman *et al.* prepared nanometre-scale $Ni(OH)_2$ clusters with high water dissociation properties on platinum electrode surfaces.[30] With a dual effect, the edges of the $Ni(OH)_2$ clusters facilitated the dissociation of water, and the produced hydrogen intermediates were then adsorbed on the nearby Pt surfaces and recombined into molecular hydrogen. Inspired by this encouraging work, various metal/metal oxide heterostructures have been fabricated. In 2014, Gong *et al.* prepared a nanoscale NiO/Ni heterostructure attached to a carbon nanotube (CNT) network, which exhibited excellent HER activity in a wide range of pH values as shown in Fig. 9a.[94] The NiO/Ni was partially reduced from $Ni(OH)_2$ through thermal decomposition. It was proposed that the exposed NiO/Ni nano-interfaces might be the synergistically active sites towards HER. Specifically, the OH^- generated by H_2O splitting could preferentially adsorb to a NiO site at the interface, while a nearby Ni site would facilitate H adsorption, boosting synergistic HER catalytic activity to NiO/Ni. In another work, Cr_2O_3 blended with NiO/Ni was later fabricated, in which the chemically stable Cr_2O_3 was essential to prevent oxidation of the Ni core and to preserve the catalytically active sites in the heterostructure, and the catalyst with heterostructure obtained great stability of more than 80 h at 200 mA cm^{-2}.[95] To date, a number of metal/metal oxide interface nanostructures have been successfully also explored, collectively showcasing that the strategy can be extended to boost the HER performance in alkaline media.[96–99]

Fabricating heterostructures based on metal oxides is also an efficient strategy to obtain remarkable OER electrocatalysts. Specifically, the metallic compounds with good conductivity and large surface area are intensively utilized as the support to improve the electron transfer process and expose active sites. For example, metallic $CoSe_2$ nanobelts were integrated with other metal oxides as a highly active and stable electrocatalyst

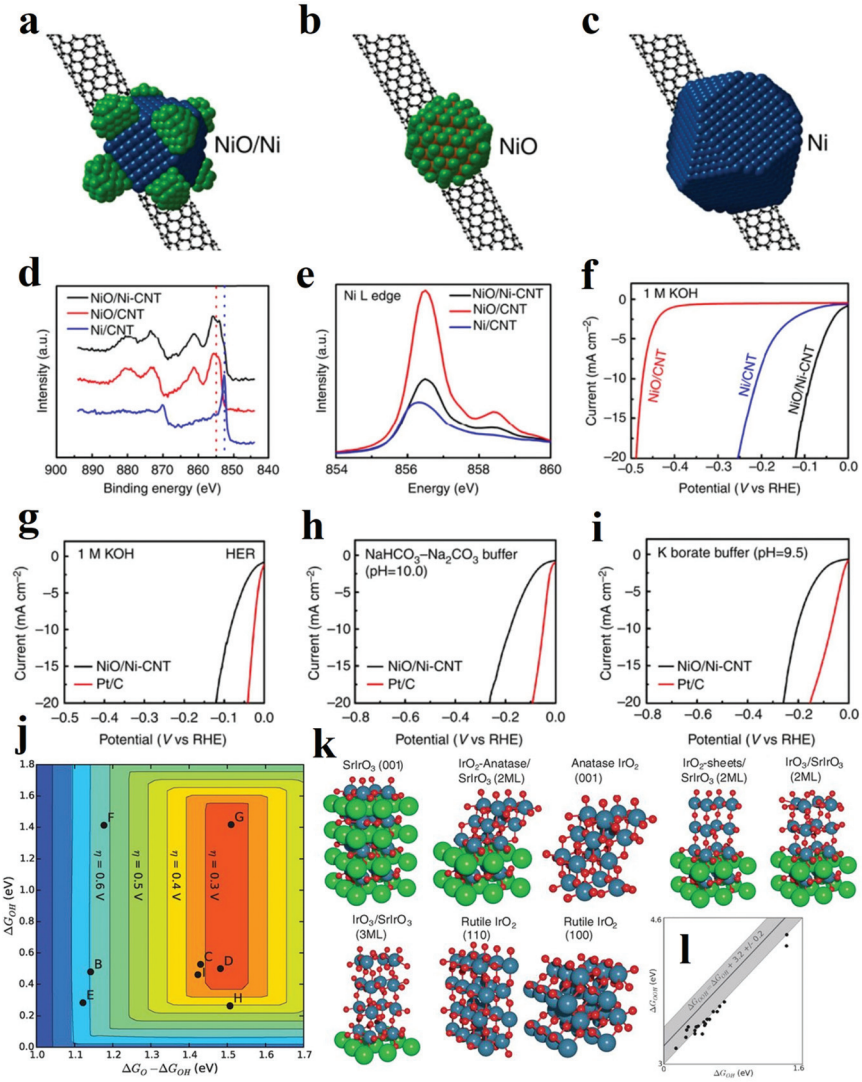

Fig. 9 (a–c) Schematic structure of (a) NiO/Ni-CNT nano-hybrid, (b) NiO/CNT, (c) Ni/CNT structure. (d) High-resolution Ni XPS spectra of the three hybrid materials. (e) Ni L edge XANES spectra of the three hybrid materials. (f) Linear sweep voltametry of the three hybrid materials in 1 M KOH. (g–i) Linear sweep voltammetry of NiO/Ni-CNT and Pt/C in (g) 1 M KOH (h) $NaHCO_3$-Na_2CO_3 buffer (pH = 10.0) and (i) potassium borate buffer (pH = 9.5).[94] (j–l) OER theoretical analysis of IrO_x/$SrIrO_3$ heterostructure. (j) Theoretical overpotential volcano plot with O* and OH* binding energies as descriptors, using the scaling relationship between OH and OOH. (k) Visual representation of IrO_x and $SrIrO_3$ surfaces used for the DFT calculations. (l) OH* and OOH* binding energies (black circles) overlaid on the universal scaling relationship (gray line with shaded uncertainty) that has been found for many transition metals and transition metal oxides.[109]

for OER.[100,101] In addition, the OER activity of pristine metal oxide is often hampered by its poor OER kinetics and mass-transfer ability while fabricating heterostructure with other metal oxides/hydroxides is proved to be an efficient strategy to optimize the energy barriers of intermediates and thus boost the catalytic activities.[102–104] Cerium(IV) oxide (CeO_2) has reversible surface oxygen ion exchange, good electronic/ion conductivity and oxygen storage capacity, and these properties are expected to enhance the catalytic performance of the electrocatalysts by altering the electrochemical reaction kinetics. For instance, electrodeposited FeOOH/CeO_2 hybrids were explored as efficient electrocatalysts for OER, exhibiting the synergistic effects between two compounds.[105] According to DFT calculations, the free energy changes of intermediates and products were lower than those free energy for CeO_2 and FeOOH. The adsorption energy of OH^- on the heterostructure was lower than those on individual FeOOH and CeO_2 surfaces, which indicated that the OH^- anions tended to be adsorbed on FeOOH/CeO_2 more efficiently, and this trait endowed the FeOOH/CeO_2 with superior catalytic activity for OER. The authors also believed that the strong electronic interaction improved durability since this heterostructure owned great stability of 50 h under 80 mA cm^{-2}. Additionally, CeO_2/Ni-TMO hybrid and CeO_2/$CoSe_2$ hybrid have also been recently fabricated, exemplifying the efficacious heterostructure methodology for high-performance electrocatalyst development.[106,107]

The heterostructure with abundant interfaces is also illustrated to improve charge transfer and to facilitate electrochemical turnover. For instance, ultrafine NiO nanosheets stabilized by TiO_2 with abundant interfaces were fabricated by annealing a monolayer layered NiTi LDH precursor.[108] It has been previously demonstrated that NiO nanosheets with a high proportion of exposed (110) facets presented efficient catalytic performance. The overall enhanced OER activity is originated from three contributing aspects. Firstly, for 3d transition metal-based electrocatalysts, the one with a surface cation e_g orbital occupancy approaching unity, shows the best performance for OER. Different from Ni^{2+} atoms in the hexagonal ultrathin bulk NiO with $t_{2g}^6e_g^2$ electron configuration, the Ni^{2+} atoms on the ultrafine and ultrathin NiO nanosheet were partially oxidized to Ni^{3+} with $t_{2g}^6e_g^1$ electronic configuration. The Ni^{3+} atoms highly exposed on (110) facets were stabilized by TiO_2 and acted as active sites with higher OER activity. Secondly, according to the DOS and the partial DOS (PDOS) results, the Ni/TiO_2 heterostructure is featured with a continuous DOS around the Fermi level, strongly indicating a high carrier concentration and good electrical conductivity. Thirdly, the adsorption energy of H_2O for this kind of heterostructure experienced a dramatic increase compared with other materials leading to the significantly enhanced OER activity. It is noteworthy that the heterostructure might form during the electrochemical OER. Thus extra attention is required when investigating the reaction mechanism and identifying the possible active sites. Seitz *et al.* thoroughly studied the formation of $IrO_x/SrIrO_3$ heterostructure in the OER test, during which Sr ions leached from the surface and minor surface rearrangement occurred.[109] The authors utilized DFT calculations to examine the activity and stability of catalyst with possible heterostructures, such as IrO_2-anatase/$SrIrO_3$, IrO_4/$SrIrO_3$, IrO_3/$SrIrO_3$ with different layer thicknesses (Fig. 9k).[109] Theoretical results indicated that IrO_2-anatase/$SrIrO_3$ and IrO_3/$SrIrO_3$ with larger IrO_3 layer thickness owned both good activity and stability. The OER performance of $IrO_x/SrIrO_3$ heterostructure is outstanding with a small overpotential of 270 to 290 mV (at 10 mA cm^{-2}), which was very near to the peak of the OER volcano. Further AFM and XPS characterizations also proved that Sr leached during OER test and thus IrO_x film *in situ* formed as active sites. Besides the metal compound hybrids, integrating the metal oxide catalysts with carbon-based materials can also enhance electrochemical reaction kinetics and dramatically boost activity through tailoring the adsorption energy of intermediates on catalysts. Li *et al.* fabricated ultrathin edge-rich FeOOH@carbon nanotubes for efficient OER.[110] The carbon nanotubes not only improved the electron transfer, but also promoted the electrochemical oxidation of oxygen species. Specifically, due to the p, π-conjugation effect of carbon atoms in graphene, oxygen atoms in FeOOH decreased the density of electron clouds around the Fe atoms. Herein, hybrid to carbon materials will enhance the adsorption of reaction intermediate on central Fe atoms, and their good electronic conductivity can also contribute to improved OER performance. However, since oxidation of carbon may occur under the OER condition, it is important not to mistake the oxidation of carbon as the OER activity.

To sum up, the synergetic effects of heterostructure can be categorized into three aspects. Firstly, the electronic structures of each composite can be efficiently modulated upon heterostructure formation. Thereby, the disassociation of water, the adsorption and desorption of the intermediates and the overall intrinsic electrochemical reaction kinetic process on the active sites are tuned and facilitated. Secondly, the heterostructures combine the unique advantages from each component and provide dual active sites at the interface, which has contributed to the excellent electrochemical performance. The support materials, especially the ones with high conductivity, can also facilitate charge transfer. Finally, some supports may mediate the growth of loaded catalytically active materials and hinder agglomerations of the nanostructured catalysts, which will contribute to higher durability. Because of the aforementioned multiple merits, heterostructure engineering has been one of the primary strategies toward the development of catalysts with high activity and excellent stability.

3.4 Heteroatom doping

With the development of nanostructure engineering in recent decades, controllable introduction of exotic atoms into a pristine atomic structure (doping) has been proven to be significantly effective in boosting the catalytic activity of active site. Depending on the type of foreign atoms, the elemental doping can be divided into cation atom doping and anion atom doping. When metal oxides are doped with foreign ions, these foreign atoms are injected into the lattice and interacted with metal oxides. The strong interactions between these dopants and the metal oxides matrix efficaciously alter the electronic structure of the oxides, which also greatly influence the electrocatalytic performance. Moreover, introduction of proton acceptors has been proved to be effective method to produce OER electrocatalysts beyond the top of volcano in AEM.

3.4.1 Cation doping. It has been reported that the electronic structures and properties can be efficiently modified by cation doping. In 2015, Xu *et al.* prepared Pr doped $Ba_{0.5}Sr_{0.5}Co_{0.8}Fe_{0.2}O_\delta$ through a facile A-site praseodymium-doping.[111] The significantly enhanced HER activity was demonstrated to be associated with the modified electronic properties, induced by the partially oxidized cobalt species and increased concentration of lattice oxygen through Pr doping. The authors confirmed the existence of oxidized cobalt species and higher concentration of lattice oxygen by XPS. They highlighted that the O atoms in the first coordination shell were with more positively charged cations, which meant these O atoms were more Lewis acidic. Therefore, through Lewis acid–base interaction, the more Lewis acidic O species promoted the adsorption of the Lewis basic H_2O. The formation of OH^- on the perovskite oxides is reflected by a hydrophobic nature that was verified by the contact angle results. In another work, Ling *et al.* also explored dual metal (Ni and Zn) doping in CoO and manifested that this doping strategy was efficient to tailor the surface and bulk electronic

structure and boost the HER activity in alkaline media.[112] Based on High-angle annular dark-field scanning transmission electron microscopy (HAADF-STEM), Energy-dispersive X-ray spectroscopy (EDS) mapping and EXAFS and DFT calculations, the authors confirmed that Ni atoms aggregated around surface oxygen vacancy and offered an ideal electronic surface structure to the binding energy of hydrogen intermediate. Meanwhile, Zn atoms inside the CoO lattice improved the bulk electronic structure, which contributed to the enhanced electrical conductivity. Another noteworthy example is the Mo–$W_{18}O_{49}$ catalysts fabricated through a wet-chemical approach by Zhong *et al.*, which manifested a small onset potential and excellent durability in acidic solution.[113] According to theoretical calculations, pristine $W_{18}O_{49}$ presented inferior HER activity because HER occurred difficultly on most of the oxygen sites, and only the oxygen on the top of W can act as active sites. In contrast, after Mo doping, the charge of oxygen atoms on the top of Mo dopants was similar to that of other oxygen atoms on W after the hydrogen adsorption, thus the Mo dopant increased the number of active sites (Fig. 10a).[113] Together with the modified electronic structure, Mo dopants resulted to an optimal hydrogen adsorption and enhanced HER activity. The following electrochemical surface area (ECSA) and EIS tests also verified the increased active sites number and the promoted charge transfer after Mo doping.

For OER, although the role of cation dopant is still unclear in improving the electrochemical reaction, cation atoms doping has been indicated to efficiently lower the kinetic energy barrier of the water dissociation step and desorption of the formed OH^- from the surface.[114–116] Recently, researches about cation doped metal oxides, such as $Zn_xCo_{3-x}O_4$ nanoarrays, Fe doped $BaCo_{0.9}Sn_{0.1}O_{3-\delta}$ and $Na_{1-x}Ni_yFe_{1-y}O_2$, demonstrated the importance of foreign cations in enhancing OER performance of metal oxides.[117–119] Fominykh *et al.* compared the OER activity of the NiO samples with different Fe dopant concentrations.[120] $Fe_{0.1}Ni_{0.9}O$ was found to demonstrate the highest electrocatalytic performance towards OER with an overpotential of 297 mV at a current density of 10 mA cm^{-2}. The Fe^{3+} doped nickel oxide for significantly enhanced OER has been well studied, and theoretical calculation demonstrated that Fe^{3+} sites provided optimal binding energy for the OH* and OOH* intermediates and worked as the active site other than Ni^{3+} sites. Meanwhile, through a *in situ* XAS experiment, Mukerjee *et al.* confirmed Fe substitutes stabilized Ni in +2 oxidation state and acted as the active sites for OER.[121] However, Li *et al.* utilized the Lewis acid–base theory to study

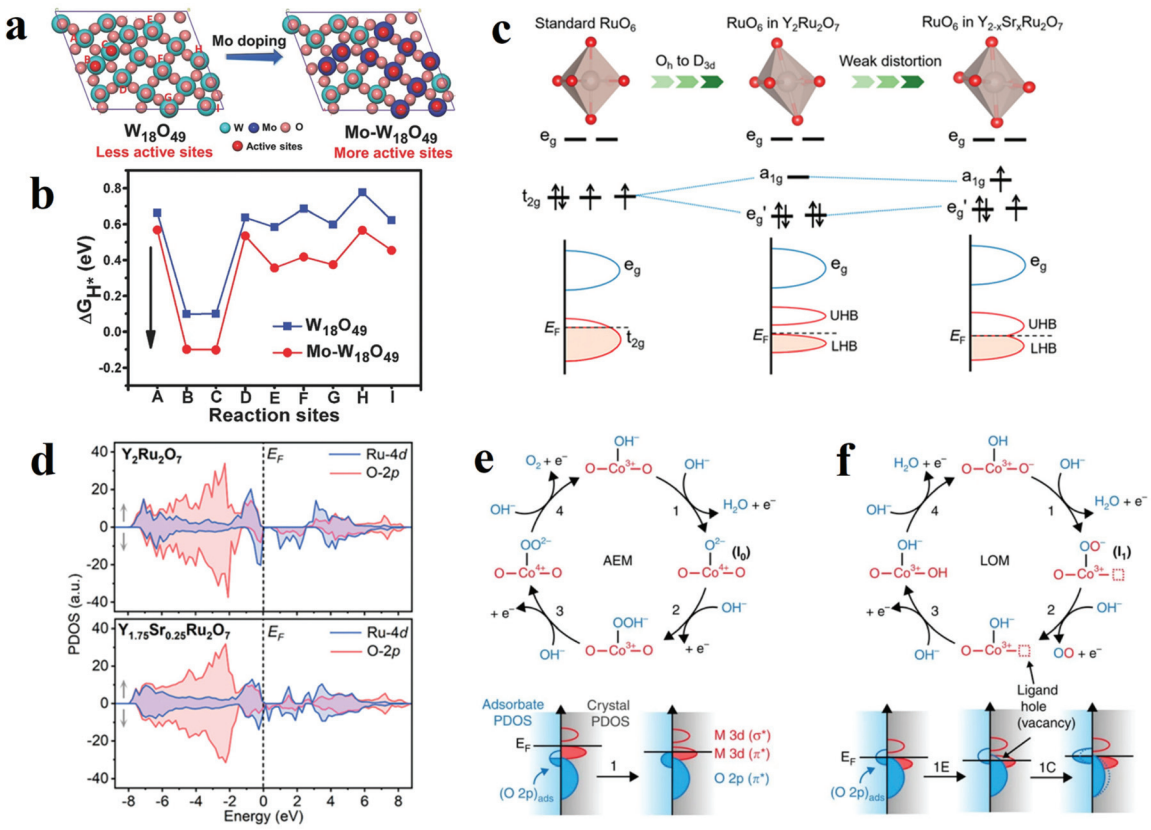

Fig. 10 (a) Different oxygen sites on $W_{18}O_{49}$ (010) and Mo–$W_{18}O_{49}$ (010). (b) The calculated Gibbs free energy of HER on different oxygen sites of $W_{18}O_{49}$ (010) and Mo–$W_{18}O_{49}$ (010).[113] (c) Schematic illustrations of different RuO_6 along with the splitting of Ru 4d orbitals. (d) Schematic evolution of band alignments through Sr^{2+} substitution for Y^{3+} in $Y_2Ru_2O_7$.[127] (e and f) Relationship between oxygen vacancy concentration and Co–O bond.[115]

the role of Fe dopant and they observed that Fe^{3+} can also function as a Lewis acid and promoted the formation of Ni^{4+} resulting to an improved catalytic performance.[122] The Fe dopant influences the Ni valency, and the formal oxidation state of Ni(IV)-oxo had a character of Ni(III)–O* resonance with an increased covalency. The oxyl radical character played a key role as oxygen radicals in O–O bond formation according to the proton-coupled electron transfer (PCET) mechanism. The research highlighted the role of Fe dopant in boosting OER activity in metal oxide catalyst. Huang and co-worker used Fe dopant to improve the OER performance of $NiCo_2O_4$ spinel materials.[123] XAS studies showed that Fe ions mainly occupied tetrahedral site of spinel lattice and induced more Ni^{3+} and Co^{2+}. The increased ratio of Ni^{3+}/Ni^{2+} and decreased ratio of Co^{3+}/Co^{2+} made the e_g occupancies of Ni and Co closer to unity, respectively, which was the optimal e_g filling for OER. Cation doping is also effective in promoting OER performance of perovskite materials. Shao-Horn's group found that the optimum e_g filling should be ~1.2 to achieve the top of the volcano plot.[46] Cation doping can finely tune the e_g filling of perovskites to achieve better performance towards OER. Based on this guidance, $SrNb_{0.1}Co_{0.7}Fe_{0.2}O_3$, $CaCu_3Fe_4O_{12}$ perovskites were explored as catalysts with good activity and stability towards OER, which were comparable or even better than state-of-art OER catalysts.[124,125] Xu's group also investigated the influence of Fe dopant on the OER performance of $LaCoO_3$.[126] With 10% Fe substitution, the spin state of Co^{3+} was transformed from a low spin state (LS: $t_{2g}^6e_g^0$) to a higher spin state, altering the catalyst characteristics from insulator to half-metal. Moreover, the change also increased overlap between Co 3d and O 2p state. Thus, M–O covalency was enhanced, which finally facilitated the OER activity. Zhang *et al.* improved the OER performance of pyrochlore ruthenate $Y_2Ru_2O_7$ in acidic medium by substituting Y^{3+} with Sr^{2+}.[127] The mass activity was 1018 A g_{Ru}^{-1} at an overpotential of 300 mV in 0.5 M H_2SO_4 electrolyte. Compared to standard RuO_6 octahedra, the RuO_6 octahedra in $Y_2Ru_2O_7$ are severely distorted, and the 4d electrons of Ru in $Y_2Ru_2O_7$ are distributed into a lower Hubbard band (LHB), resulting in the upper Hubbard band (UHB) empty. This Mott–Hubbard splitting phenomenon impedes the charge transfer between active sites and intermediates, resulting in an inferior OER performance. For the $Y_{1.7}Sr_{0.3}Ru_2O_7$ catalyst, the exotic Sr^{2+} cations on one hand can regulate coordination geometry and charge redistribution. From the results of XRD Rietveld refinement and Raman spectra, the bond angle of Ru–O–Ru increased from 128.2° to 129.8° after Sr substitution, which alleviated the distortion of RuO_6 moieties and improved the overlap of Ru 4d and O 2p orbitals (Fig. 10c).[127] On the other hand, the Sr substitution also increased the Ru valence and facilitated the charge transfer from oxygen ligand to Ru centre, which also resulted in enhanced orbital hybridization and bond covalency (Fig. 10d).[127]

It should be noticed that substitution is the effective method to produce OER electrocatalysts beyond the top of the volcano in AEM. For example, substitution by metals with higher electronegativity can act as proton acceptors. Halck *et al.* utilized the incorporation of Ni and Co into RuO_2 surface to improve the OER performance.[128] According to the reaction pathway and scaling relationship in AEM, the smallest overpotential for OER would be 0.4 V. However, after substitution of Ru by Ni and Co, the oxygen atoms on the bridge positions were activated and acted as a proton acceptor. Unlike the traditional scaling relation of HOO* and HO*, the adsorption free energy difference between HOO* and HO* was changed. As a result, the overpotentials for Co- and Ni-substituted RuO_2 were only *ca.* 0.1 V and 0.25 V, respectively. In addition, cation substitutions can also promote OER with the LOM mechanism. Stevenson *et al.* first proposed the LOM mechanism by using Sr substitution into $La_{1-x}Sr_xCoO_{3-\delta}$.[115] The covalency of the Co–O bond and the concentration of oxygen vacancies can be regulated by controlling Sr substitution (Fig. 10e and f).[115] It was demonstrated that the transition from AEM to LOM occurred when $x \geq 0.4$. With increasing Sr substitution, the oxidation state of Co was also increased, which led to a more significant overlap between Co 3d and O 2p orbitals and the formation of π^* and σ^* bands. When the overlap was great enough, ligand holes (oxygen vacancies) were formed, and the Co 3d π^* band cannot be treated as an energy level isolated from the oxygen 2p π^* band. Therefore, the Fermi energy can be modulated by controlling Co–O covalency, and thus Sr substitution provided the opportunity for lattice oxygen redox activity. The formation of superoxide-like –OO *via* the coupling of lattice oxygen and adsorption oxygen finally resulted in fast OER kinetics.

3.4.2 Anion doping. Besides cation doping, various anion dopants, such as N, P, and S have been utilized to prepare anion-doped metal oxides as effective water-splitting catalysts. Introduction of anion dopant enhance the electronic conductivity and modify the adsorption strength of intermediates, finally resulting in the improvement of the reaction kinetics.

In 2017, Xiao *et al.* developed a facile strategy to fill the oxygen vacancies in the Co_3O_4 with phosphorus by thermal coupled plasma modification approach.[129] The electrocatalytic performance of P-Co_3O_4 for HER and OER was much better than these of pristine Co_3O_4 and V_O-Co_3O_4 (V_O = oxygen vacancies). The overpotential of overall water splitting was only 420 mV at 100 mA cm^{-2} in 5 M KOH electrolyte. The electronic properties of the P-Co_3O_4 have been investigated through both theoretical calculation and experiments. By comparing XAS results of P-Co_3O_4 and V_O-Co_3O_4, P dopants were confirmed to fill into the O-vacancies. When V_O was formed, electrons transferred into Co 3d orbitals, preferably forming $Co^{3+}{}_{Oh}$, instead of $Co^{2+}{}_{Td}$. While with P dopants in the O-vacancy site, electrons transferred out of Co 3d states, and thereby the number of $Co^{2+}{}_{Td}$ sites (with better HER and OER catalytic activity) increased. More importantly, P-filling can also significantly improve the intermediate binding, hence remarkably boost the HER and OER activity. According to the calculated free energy diagram for HER, P-Co_3O_4 has a favourable ΔG_{H^*} of −0.08 eV. The free energy profiles along the OER process also demonstrated enhanced binding strength of O* and OOH* intermedi-

ates on P-Co_3O_4. Co_3O_4 with P-doping showed superior OER performance to pristine Co_3O_4. Nitrogen doped molybdenum trioxide (N-doped MoO_3) was fabricated by heating commercial MoO_3 at NH_3 atmosphere and exhibited 6 times higher activity towards HER than intact MoO_3.[130] Positron annihilation spectrometry (PAS) confirmed that the N-doping induced increased concentration of V_OV_O divacancies, which might be the active sites for HER. Further DFT calculations verified that the existence of V_OV_O divacancies improved the state density near the valence band edge and thereby boosted the catalyst's electronic conductivity.

Anion doping can be facile to improve electrocatalytic performance of metal oxides in terms of activity and durability of OER. Through solid-state reaction, P doped $SrCoO_{3-\delta}$ (SCP) perovskite has been fabricated and showed high OER performance benefiting from its high electrical conductivity and large amount of OO^{2-}/O^- species.[131] The doping of high-valence-state P^{5+} in SCP resulted in charge compensation and boosted the electrical conductivities. Importantly, compared to $SrCoO_3$, P doped $SrCoO_{3-\delta}$ showed better durability which can be attributed to the stable tetragonal structure after P-doping. Controllable nitrogen doped cobalt oxides (N-Co_3O_4 and N-CoO) were synthesized from cobalt-alanine complexes by calcination at different atmosphere.[132] The authors highlighted the OER performance of N-Co_3O_4, which required overpotential of only 190 mV at 10 mA cm^{-2} and showed the smallest Tafel slope of 29.8 mV dec^{-1} in 1.0 M KOH. The authors, through DFT calculations, claimed that N-doping can not only improve the OH-adsorption capability, but also facilitate OH-cleavage. Moreover, N-doping also reduced the bandgap from 1.80 eV to 1.42 eV, which made the excitation of charge carriers to the conduction band easier and improve the electronic conductivity. Sulphur doped cobalt oxide ($CoO_{0.87}S_{0.13}$/GN) was also investigated to explore the benefit of anion doping to the electrochemical reaction performance.[133]

3.4.3 Single atomic catalysts. The recent growth in research on catalysis by atomically dispersed metal atoms indicated the rising research interest in the heterogeneous catalysis. Single atom catalysts (SACs) represent isolated individual metal atoms anchored on or coordinated with the surface atoms of a proper support, which can be seen as another category of doping. SACs can provide an alternative strategy to maximize the atom utilization efficiency of metals and precisely tune the activity and selectivity of the catalytic reaction.

It is acknowledged that the heterogeneous electrocatalytic process only occurred on the surface of the electrocatalysts, and the activities of the electrocatalysts are determined by their size and the accessible active sites. Therefore, preparing electrocatalyst in atomic scale will contribute to the enlarged exposure of the active sites and thus enhance electrochemical activity. Recently, Dou *et al.* prepared atomic-scale CoO_x species through on-site transformation of the atomically distributed Co^{2+} in ZIF-67 by O_2 plasma treatment.[134] Benefiting from the large surface area and abundant exposed active species, the electrocatalyst exhibited remarkable OER performance.

In addition, metal oxide is usually utilized as the support to promote the distribution of the electrocatalytic active species. Especially used for selective activation of methane or CO oxidation, various single atom noble metals supported on metal oxide are intensively explored with remarkably enhanced catalytic performance.[135,136] More recently, Nong *et al.* prepared Ru doped TiO_2, in which the penta-valence Ru atom was homogeneously distributed in the lattice.[137] The experiment and PDOS calculation confirmed that the Ru^{5+} existed in a row of $-RuO_3$ in the surface of TiO_2, which was defined as TiO_2:Ru_{surf}. According to the DFT calculation, the adsorption of hydrogen is preferred on the TiO_2:Ru_{surf} structure with increase of hydrogen coverage and the calculated ΔG_H on these sites was −0.28 eV, suitable for HER.

To sum up, elemental doping can be a facile and effective method in boosting the electrochemical performance of metal oxides. Dopants can regulate the charge transfer properties and intermediate adsorption energy by modifying the bulk electronic structure, spin state of metal site, and M–O covalency. Besides, some dopants, especially the metals with higher electronegativity, can serve as proton acceptor. These dopants can introduce lattice oxygen, and thus produce efficient OER catalyst following LOM instead of AEM, providing opportunities to break the scaling relation. Finally, some dopants are the efficient active sites by themselves, especially for cases of cation doping and single atom doping.

3.5 Defect and strain engineering

Atomic discontinuity in nanoscale in metal oxides, metal sulphides and metal selenides have demonstrated as active sites. Thus defect, and strains enriched metal related compounds have been applied to various electrochemical reaction.[138–140]

3.5.1 Cation defects. Great efforts have been devoted to the investigation of control over cation defects in transition metal oxide catalysts. Zhang *et al.* investigated the effects of cation defects in Co_3O_4 on the OER performance.[141] The $Co_{3-x}O_4$ samples were prepared by simply calcinated the Co_3O_4 precursor at different temperatures, namely 300 °C (Co-300), 500 °C (Co-500) and 700 °C (Co-700). The abundant Co defects were confirmed by performing XANES and EXAFS, and results indicated that the Co-300 possessed the largest amount of Co defects. The Co-300 exhibited a superior performance for OER than IrO_2 and RuO_2, with a small overpotential of 268 mV at 10 mA cm^{-2}. As illustrated through experimental and theoretical results, Co vacancies caused electronic delocalization structure and facilitated electrical conductivity. Therefore, the electrical resistance of Co-300 samples (100.5 Ω) was much lower than those of Co-500, Co-700, IrO_2 and RuO_2. On the other hand, due to the presence of Co vacancies on $Co_{3-x}O_4$, the adsorbed energy of water was lower than that of stoichiometric Co_3O_4, which could be verified by the better wettability of Co-300. Chen *et al.* also reported the influence of Sn vacancies on $SnCo_{0.9}Fe_{0.1}(OH)_6$ by Ar plasma treatment.[142] Due to the weak $Sn(OH)_4$ bond, abundant Sn vacancies formed after Ar plasma. The large amount of Sn vacancies resulted in an amorphous surface and exposed more CoFe active sites.

Moreover, the defects also decreased the coordination number of CoFe active sites, and efficiently tuned the surface electronic structure. The O* adsorption on Co site (2.49 eV) was therefore optimized, and a much lower overpotential (0.43 V) was achieved.

3.5.2 Anion defects. Anion defect engineering was explored to improve the catalytic performance of transition metal oxides for HER and OER. Li *et al.* prepared the $WO_{2.9}$ by simply heating commercial WO_3 powder in a reduction atmosphere.[143] The non-stoichiometric $WO_{2.9}$ showed excellent electrocatalytic activity for HER, and the overpotential was merely −70 mV at 10 mA cm^{-2} in acidic water. The reaction mechanism was further investigated by examining $WO_{2.9}$ (010) and WO_3 (001), which were the most stable surfaces for $WO_{2.9}$ and WO_3 (Fig. 11a and b).[143] Compared to WO_3 (001), the $WO_{2.9}$ (010) possessed a largely enhanced adsorption energy for atomic hydrogen and obtained a better catalytic activity. In another work, Qiao's group created oxygen vacancies on the oxygen-terminated (111) pyramidal nanofacets of single crystal CoO nanorods (SC CoO NRs).[144] These CoO nanorods with rich oxygen vacancies possessed superior catalytic activity and durability towards OER. The SC CoO NRs achieved a current density of 10 mA cm^{-2} at 1.56 V and a Tafel slope of 44 mV dec^{-1} in 1 M KOH solutions for OER. As shown in Fig. 11c,[144] after the introduction of O-vacancy into CoO, new electronic states were created (indicated by the arrow in Fig. 11c) by the hybridization of O 2p, Co 3d, and Co 3s in the bandgap. These new electronic states contributed to the modulation of adsorption energy of intermediates and better electronic conductivity. Therefore, O-vacancies improved the overall electrode activity of SC CoO NRs for OER.

3.5.3 Strain engineering. Strain engineering is also an efficient method to modify key structure features like the M–O bond and to optimize the adsorption–desorption energetics of intermediates through controlling defects.[145] Strain, also known as lattice strain, is derived from geometric lattice distortion, and thereby can be observed and defined by geometric phase analysis.[146] One can induce strain through the introduction of lattice distortion by growing metal oxide on lattice-mismatched substrates or by cation exchange to create abundant vacancies.[146,147] Therefore, the strain can be tuned by changing the substrates or changing the reaction conditions of cation exchange. Qiao's group designed cobalt(II) oxide nanorods with different surface strains and obtained efficient electrocatalysts for HER.[146] The synthesized CoO NRs with 3% strain displayed a small overpotential of 73 mV at 10 mA cm^{-2} in 1 M KOH, which was comparable to that of noble metal catalysts. As illustrated in Fig. 11e,[146] ΔG_{H^*} on typical CoO was

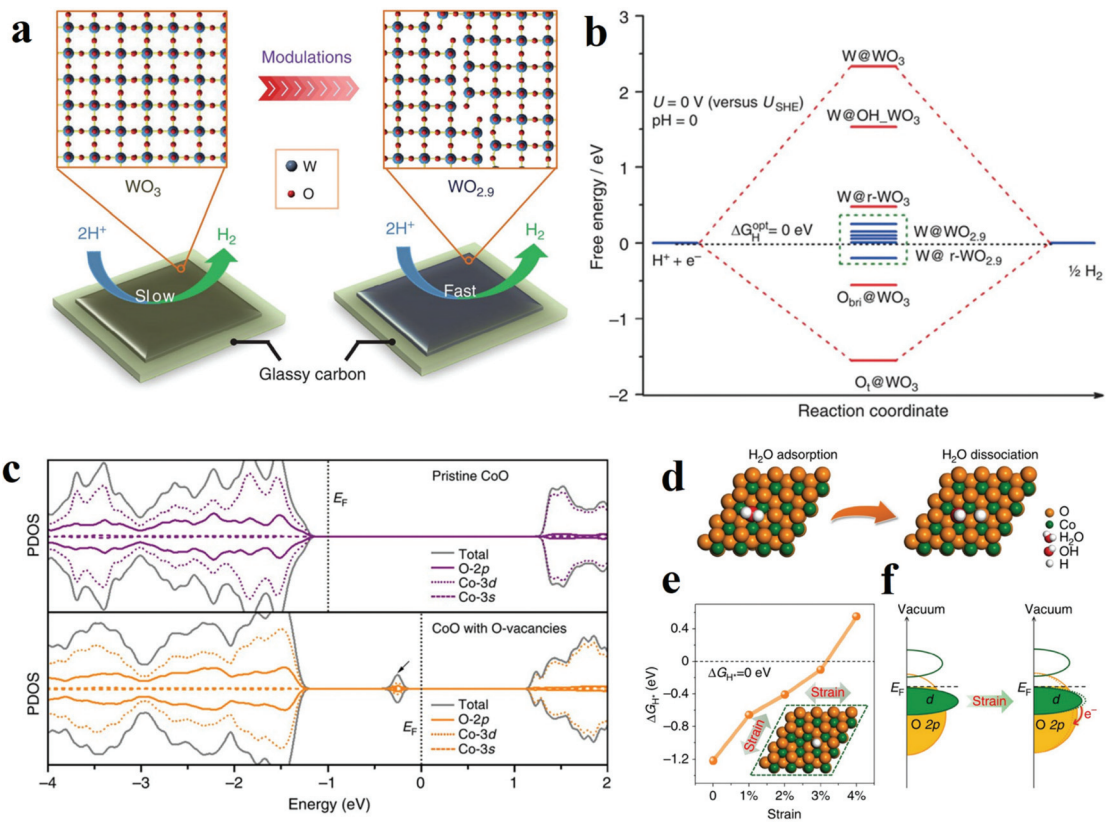

Fig. 11 (a and b) Plausible reaction mechanism and DFT calculation results of electrocatalytic H_2 evolution on $WO_{2.9}$.[143] (c) The projected density of states (PDOS) on pristine CoO and (d) CoO with O-vacancies.[144] (d–f) Computational predictions for the strain effect on the HER activity of CoO.[146] (d) Schematic illustration of H_2O adsorption and dissociation on the CoO (111) surface with O-vacancies (e) hydrogen adsorption free energy, ΔG_{H^*}, *vs.* tensile strain for the CoO (111)-O_v surface. (f) Schematic illustration of the effect of strain on the electronic structure of (111)-O_v surface of CoO.

too negative indicating an unfavored H* desorption. The introduced strain can modulate ΔG_{H^*}, and 3.0% strain could be the optimal value since the corresponding ΔG_{H^*} was close to 0 eV (Fig. 11f).[146] The presence of strain upshifted O 2p band, which increased the overlap of Co d band and O 2p band and made Co–O covalency greater. Therefore, surface O atoms bound more strongly to surrounding Co atoms and it became unlikely for them to accept electrons from H*. As a result, the H adsorption became weaker. Petrie *et al.* also used the same strategy to control O-vacancies in perovskites by tuning strain.[147] They applied epitaxial strain on perovskite $SrCoO_{3-\delta}$ (P-SCO) film to control the oxygen defects. The results showed the catalytic performance of P-SCO with 4.2% tensile strain for OER was comparable to that of IrO_2. With the tensile strains changing from 1% to 4.2%, the $SrCoO_{3-\delta}$ varied from $SrCoO_{2.9}$ to $SrCoO_{2.75}$. The anodic scan and galvanostatic measurements indicated that the tensile strain facilitated the oxygen vacancy generation. It was also observed that the concentration of Co^{3+} ions, which were the active sites for OER, increased with the growing tensile strain. Therefore, as illustrated, the application of optimized tensile strain would increase the concentrations of both oxygen vacancies and Co^{3+} ions resulting to enhanced catalytic performance. On the other hand, strain with different directions also have a distinctive influence on the orbital overlap, which will further impact charge transport properties and intermediate adsorption energies. Tensile strain and compressive strain conduce to filling the in-plane ($d_{x^2-y^2}$) and out-of-plane (d_{z^2}) orbitals.[148,149] Lee's group applied different strain ranging from −2.2% to 2.7% to $LaNiO_3$ by depositing $LaNiO_3$ on a range of lattice-mismatched substrates.[150] When the compressive strain was applied, the e_g-centre moved toward lower energies (a weaker M–O chemisorption) and further enhanced OER catalytic activity.

In general, defect engineering in metal oxides mainly focus on the control over oxygen vacancies and metal site vacancies. By tuning vacancies, the charge transfer ability and adsorption energy of reactants and intermediates are optimized, thus, the intrinsic catalytic activity of active site is improved. In addition, when the defects accumulate to an exact extent, amorphization may be introduced, and more active sites can be exposed. Strain engineering can also control the vacancies and achieve similar results of anion defect engineering. Also, expansion and compression of catalyst lattice allows modulation in electronic structure towards optimal catalytic activity.

3.6 Amorphization

Amorphization has been proved to be an effective and general strategy to engineer the surface structure of catalysts. The strategy has been widely used in facilitating a variety of catalysts, such as transition metal oxides, sulfides and phosphides.[151–153] Partial and complete loss of long-range crystalline structure in to disordered phases will expose more catalytic active site and modulate the electron structure.

Indra *et al.* compared the electrochemical catalytic activity of amorphous and crystalline cobalt iron mixed metal oxides for OER and ORR.[154] It was found that the amorphous $CoFe_2O_4$ can achieve a current density of 10 mA cm^{-2} with a small overpotential of 490 mV for OER, which was 70 mV lower than that of crystalline one. The authors considered that the better activity was from amorphous surface which exposed more Co^{3+} active sites and owned higher specific surface area. In 2014, Geng's group reported an aerosol-spray-assisted fabrication of amorphous metal oxides with precise control over compositions and structures.[155] Among all the Fe–Ni–O_x prepared, $Fe_6Ni_{10}O_x$ showed the best performance for electrochemical water oxidation, with a low overpotential of 0.286 V at 10 mA cm^{-2} under alkaline conditions. The effect of crystalline phase on electrochemical water oxidation by calcining the samples in different temperatures was further investigated. The results showed that the superior electrochemical catalytic activity of amorphous phase derived from its larger capacitance, which indicated the amorphous phase possessed a larger ECSA. Other authors also drew the similar conclusion that the large surface specific area of amorphous phase was the origin of improvement in electrochemical catalytic performance for OER.[156,157]

In general, compared with the crystalline phase, the amorphous phase obtains a larger surface specific area and thereby exposes more active sites.[156] Besides, the amorphous surface possesses a high concentration of active sites, which play an important role in enhancing the adsorption of reactants and optimizing the coverage of intermediates.[158]

3.7 *In situ* transformation

Recently, metal phosphides, sulfides, and selenides *etc*. are reported as extraordinary catalysts towards water-splitting.[159–161] However, one should be very careful when determining the real active phase especially under OER conditions, since these electrocatalysts often experience complete or partial oxidation, and could be transformed into inhomogeneous materials when OER occurs.[162] Therefore, composition and structure studies on these catalysts *via ex situ* method may not accurate when identifying the active phases, and it should be more appropriate to name these catalysts as pre-catalyst. The active phases are usually composed of oxides, which are formed under OER conditions and lead to an enhancement in catalytic performance. Overall, *in situ* transformation is a useful method to obtain metal oxides from phosphides, nitrides, sulfides, and selenides *etc*.

Hu's group reported Ni_2P/NiO_x catalysts with the core–shell structure derived from Ni_2P particles towards overall water-splitting.[163] The Ni_2P/NiO_x delivered a current density of 10 mA cm^{-2} with an overpotential of only 290 mV in alkaline electrolyte. The partial oxidation of Ni_2P generated NiO_x shell, which served as the active part towards OER. The Ni_2P core acted as conducting support and provided favourable electron transfer pathway to the NiO_x. The author declared there might be synergistic effects between these two parts, which needed further study. In another work, $NiFeO_x$ nanosheet was *in situ* transformed from $NiFeSe_2$ nanoplate by implying a galvanostatic scan of 5 mA cm^{-2}.[164] The as-prepared catalyst exhibited a small overpotential of 195 mV at 10 mA cm^{-2} and a good stability of 24 h under 10 mA cm^{-2}. From TEM images and EDS

Table 1 Summary of fabrication strategies for some selected metal oxide electrocatalysts and their performance towards water splitting

Strategy	Electrocatalyst/substrate[a]	Mass loading (mg cm^{-2})	Reaction	Electrolyte	η_{10} (mV)	Tafel slope (mV dec^{-1})	Stability	Ref.
Nanoscale confinement	$NiFeO_x$ nanoparticles/CFP	3	HER	1 M KOH	88	150	100 h (@10 mA cm^{-2})	73
			OER		230	31.6		
			Water splitting		280	N.A.		
	$LiCo_{0.33}Ni_{0.33}Fe_{0.33}O_2$ nanoparticles/CFP	~0.1	OER	0.1 M KOH	340	73.6	1000 cycles	74
	80 nm-$LaCoO_3$/GC	0.25	OER	0.1 M KOH	490	69	3 h (@10 A g^{-1})	75
	Co_3O_4 nanosheets/GC	0.34	OER	1.0 M KOH	790 (@341.7 mA cm^{-2})	25	10 000 cycles	76
	γ-CoOOH nanosheets/GC	~0.15	OER	1.0 M KOH	300	38	13 h (@10 mA cm^{-2})	77
	Co_3O_4 microtubes/Ni foam	N.A.	HER	1.0 M KOH	170	98	12 h (@20 mA cm^{-2})	79
			OER		260 (@150 mA cm^{-2})	84		
			Water splitting		400	N.A.		
	Co_3O_4 nanotubes/GC	0.208	OER	0.1 M KOH	390	76	2000 cycles/40 h (@20 mA cm^{-2})	80
	$NiCo_2O_4$ hollow microcuboids/Ni foam	~1	HER	1.0 M NaOH	−110	49.7	36 h (@20 mA cm^{-2})	81
			OER		290	53		
			Water splitting		420	N.A.		
	Ni–Co_2–O hollow nanosponges/GC	0.2	OER	0.1 M KOH	362	64.4	500 cycles	82
Crystal phase and facet engineering	γ-Ti_2O_3 film/(001)$SrTiO_3$	N.A.	HER	0.5 M H_2SO_4	271	199	N.A.	85
	MnO_x film/FTO or Au	N.A.	OER	1.0 M NaOH	N.A.	63	N.A.	86
	Co_3O_4@CoO nanocubes/GC	~0.025	OER	0.5 M KOH	430	89	1000 h (@8 mA cm^{-2})/6000 cycles	88
				0.5 M Na_2SO_4	851	375		
	$BaNi_{0.83}O_{2.5}$/GC	0.295	OER	0.1 M KOH	~380	N.A.	1000 cycles	89
	(110) $NiCo_2O_4$ nanosheets/Ni foam	1.12	HER	1.0 M KOH	157 (@5 mA cm^{-2})	71.2	50 h (@5 mA cm^{-2})	90
			OER		330 (@5 mA cm^{-2})	59.2		
			Water splitting		360	N.A.		
	(112) Co_3O_4 nanoparticles/GC	0.15	OER	0.1 M KOH	380	62	~7 h(@1 mA cm^{-2})	91
	(012)-O α-Fe_2O_3/CFP	0.014	OER	1.0 M NaOH	317	58.5	30 h (@10 mA cm^{-2})	92
	$LaCoO_3$ (100) film/GC	N.A.	OER	1.0 M KOH	470	180	20 000 s	93
Heterostructure	$Ni(OH)_2$-Pt/GC	N.A.	HER	0.1 M KOH	100	100	N.A.	30
	NiO-Ni/CNT	0.28	HER	1.0 M KOH	<100	82	20 h (@−20 mA cm^{-2})	94
	Ni@Cr_2O_3-NiO/Ni foam	8	HER	1.0 M KOH	115 (@100 mA cm^{-2})	N.A.	80 h (@−200 mA cm^{-2})	95
	CoO_x@CN/GC	1	HER	1.0 M KOH	232	115	9000 s (@10 mA cm^{-2})	96
			OER		260	N.A.		
			Water splitting		320(@20 mA cm^{-2})	N.A.		
	$Ni(OH)_2$-Pt/GC	N.A.	HER	0.1 M KOH	100	100	N.A.	30
	NiO-Ni/CNT	0.28	HER	1.0 M KOH	<100	82	20 h (@−20 mA cm^{-2})	94
	Ni@Cr_2O_3-NiO/Ni foam	8	HER	1.0 M KOH	115 (@100 mA cm^{-2})	N.A.	80 h (@−200 mA cm^{-2})	95
	CoO_x@CN/GC	1	HER	1.0 M KOH	232	115	9000 s (@10 mA cm^{-2})	96
			OER		260	N.A.		
			Water splitting		320(@20 mA cm^{-2})	N.A.		
	Ni/NiO-NSAs/Ni foam	0.59	HER	0.1 M KOH	~230	114	10 h	97
	Ni-CeO_2/CNT	0.14	HER	1.0 M KOH	<100	N.A.	10 h(@−0.153 V)	98

Table 1 *(Contd.)*

Strategy	Electrocatalyst/substrate[a]	Mass loading (mg cm^{-2})	Reaction	Electrolyte	η_{10} (mV)	Tafel slope (mV dec^{-1})	Stability	Ref.
	Co-Co_3O_4/Ni foam	0.85	HER	1.0 M KOH	90	44	6000 s (@−0.120 V)	99
	Mn_3O_4-$CoSe_2$/GC	~0.2	OER	0.1 M KOH	~350	49	12 000 cycles	100
	CoO-$CoSe_2$/Ti	~2	HER	0.5 M PBS	337	131	10 h	101
			OER		510	137		
			Water splitting		950			
	Mn_3O_4@$Mn_xCo_{3-x}O_4$/Ni foam	0.3	OER	1.0 M KOH	246	46	40 h	102
	Co_3O_4-$NiCo_2O_4$/Ni foam	1	OER	1.0 M KOH	340	88	12 000 cycles	103
	NiO-Co_3O_4/NC	0.2	OER	1.0 M KOH	240	73	48 h	104
	FeOOH-CeO_2/Ni foam	N.A.	OER	1.0 M NaOH	~240	N.A.	50 h (@80 mA cm^{-2})	105
	CeO_2-CoSe/GC	0.2	OER	0.1 M KOH	288	44	10 h (@10 mA cm^{-2})	106
	CeO_2-TMO/Ni	N.A.	HER	1.0 M KOH	93	69	30 h (@10 mA cm^{-2})	107
			OER		220	38		
			Water splitting		350	N.A.		
	NiO/TiO_2	0.34	OER	1.0 M KOH	320	52	10 h	108
	IrO_x/$SrIrO_3$ film	N.A.	OER	0.5 M H_2SO_4	270	N.A.	30 h (@10 mA cm^{-2})	109
	FeOOH/CNTs	0.05	OER	1.0 M KOH	206	31	10 h (@10 mA cm^{-2})	110
Heteroatom doping	$Pr_{0.5}(Ba_{0.5}Sr_{0.5})_{0.5}Co_{0.8}$, $Fe_{0.2}O_{3-\delta}$/GC	0.232	HER	1.0 M KOH	237	45	25 h (@−50 mA cm^{-2})	111
	Ni,Zn-CoO/CFP	N.A.	HER	1.0 M KOH	53	47	24 h (@−10 mA cm^{-2}, 6 M KOH)	112
	Mo–$W_{18}O_{49}$/GC	0.16	HER	0.5 M H_2SO_4	45	54	10 h (@−0.14 V)	113
	$Sr_{0.90}Na_{0.10}RuO_3$/GC	0.1	OER	0.1 M $HClO_4$	170	40	N.A.	114
	$La_{1-x}Sr_xCoO_{3-\delta}$/GC	0.051	OER	0.1 M KOH	~370	31	10 h (@10A g^{-1})	115
	$LiCo_{0.8}Fe_{0.2}O_2$/GC	0.232	OER	0.1 M KOH	340	50	6 h (@10 mA cm^{-2})	116
	$Na_{1-x}Ni_yFe_{1-y}O_2$/GC	0.13	OER	1.0 M KOH	260	44	30 h (@10 mA cm^{-2})	117
	$Zn_xCo_{3-x}O_4$/Ti	N.A.	OER	1.0 M KOH	320	51	~2 h (@1.63 V)	118
	$BaCo_{0.9-x}Fe_xSn_{0.1}O_{3-\delta}$/GC	0.232	OER	0.1 M KOH	~390	69	2 h (@5 mA cm^{-2})	119
	$Fe_{0.1}Ni_{0.9}O$/Au	N.A.	OER	0.5 M KOH	297	37	10 h(@10 mA cm^{-2})	120
	$Ni_{0.8}Fe_{0.1}Co_{0.1}O$/GC	0.25	OER	0.1 M KOH	~410	N.A.	N.A.	121
	Fe-$NiCo_2O_4$/FTO	N.A.	OER	1.0 M NaOH	201	39	N.A.	122
	$SrNb_{0.1}Co_{0.7}Fe_{0.2}O_3$/GC	0.232	OER	0.1 M KOH	420	76	1000 cycles	124
	$CaCu_3Fe_4O_{12}$/GC	0.25	OER	0.1 M KOH	310	51	100 cycles	125
	$Y_{2-x}Sr_xRu_2O_7$/GC	0.071	OER	0.5 M H_2SO_4	264	44.8	28 h (@−10 mA cm^{-2})	127
	P-Co_3O_4/Ti mesh	N.A.	HER	1.0 M KOH	120	52	~2 h (@1.64 V)	129
			OER		280	51.6		
	N-MoO_3/GC	0.694	HER	0.5 M H_2SO_4	210	101	1000 cycles	130
	$SrCo_{0.95}P_{0.05}O_{3-\delta}$/GC	0.232	OER	0.1 M KOH	480	84	1000 cycles	131
	N-Co_3O_4/Ni foam	0.25	OER	1.0 M KOH	190	30	1.11 h	132
	$CoO_{0.87}S_{0.13}$/graphene nanomesh	0.36	OER	0.1 M KOH	360	N.A.	3000 cycles	133
	CoO_x-ZIF/GC	~0.2	OER	1.0 M KOH	318	70.3	2000 cycles	134
	TiO_2:Ru/GC	~0.2	HER	0.1 M KOH	150	97	1000 cycles	137
Defect and strain engineering	$Co_{3-x}O_4$/GC	N.A.	OER	1.0 M KOH	268	38.2	2000 cycles	141
	$Sn_{1-x}Co_{0.9}Fe_{0.1}(OH)_6$/GC	~0.1	OER	1.0 M KOH	270	42.3	2000 cycles	142
	$WO_{2.9}$/GC	0.285	HER	0.5 M H2SO4	70	50	~4 h (@−1.64 V)	143
	CoO/CFP	~0.19	OER	1.0 M KOH	330	44	N.A.	144
	3.0% S-CoO/CFP	~0.46	HER	1.0 M KOH	73	83	28 h (@−0.073 V)	146
	4.2% S-$SrCoO_{3-\delta}$/GC	N.A.	OER	0.1 M KOH	~330	40	~3 h (@5 μA)	147
	S-$LaNiO_3$/GC	N.A.	OER	0.1 M KOH	~350	N.A.	N.A.	150

Table 1 *(Contd.)*

Strategy	Electrocatalyst/substrate[a]	Mass loading (mg cm^{-2})	Reaction	Electrolyte	η_{10} (mV)	Tafel slope (mV dec^{-1})	Stability	Ref.
Amorphization	IrO_x/FTO	0.0001	OER	1.0 M H_2SO_4	190	34	24 h (@1 mA cm^{-2})	151
	$CoFeO_x$/GC	0.051	OER	0.1 M KOH	490	N.A.	N.A.	154
	$Fe_6Ni_{10}O_x$/GC	0.1	OER	1.0 M KOH	286	48	N.A.	155
	$VFeCoO_x$/GC	0.28	OER	1.0 M KOH	307	36	12 h (@−1.55 V)	156
In situ transformation	Ni_2P/NiO_x/GC	0.14	OER	1.0 M H_2SO_4	290	47	10 h (@10 mA cm^{-2})	163
	$NiFeO_x$ nanosheet/Ni foam	N.A.	OER	0.1 M KOH	195	28	24 h (@10 mA cm^{-2})	164
	$CoNiFeO_x$/carbon fibre cloth	N.A.	OER	1.0 M KOH	232	38	100 h (@20 mA cm^{-2})	165

[a] CFP = carbon fibre paper; GC = glassy carbon; FTO = fluoride doped tin oxide; CNT = carbon nanotube; NC = nitrogen-doped carbon.

mapping results, the precursor nanoplate $NiFeSe_2$ was entirely converted into $NiFeO_x$, and the obtained oxide maintained the nanosheet morphology with only 1–2 nm thickness. Benefiting from the ultrathin nanosheet morphology and Ni–Fe synergic effect, the $NiFeO_x$ outperformed NiFe LDH and even other benchmark catalysts. In addition, Cui *et al.* utilized *in situ* oxidation to develop binary, ternary, and quaternary transition metal oxide from sulfides.[165] Impressively, $CoNiFeO_x$ grown on carbon fibre exhibited a small overpotential of 232 mV at reach 10 mA cm^{-2} and extraordinary durability of more than 100 h, outperforming most of other non-noble OER catalysts.

Overall, *in situ* transformation is an effective method to obtain metal–oxide-based catalysts with good performance. Firstly, the metal oxides normally possess analogous morphology to their pre-catalyst counterparts, and the specific morphology would substantially boost the electrocatalytic activity. Secondly, partial *in situ* oxidation may produce specific core–shell heterostructures, and the synergic effect between these two different parts may be beneficial to the enhanced overall electrocatalytic performance. In addition, the anion elements of the pre-catalysts inevitably undergo leaching into the electrolytes. Thus, the resultant true electrocatalysts are endowed with higher specific areas and more exposed active sites which benefit the electrocatalytic turnovers.

Taken together, this part of the review has surveyed strategies towards modulations of the morphology, composition, and structure of metal oxide electrocatalysts. A summary of the high-performance metal oxide electrocatalysts towards water splitting developed by these strategies is given in Table 1. Generally, by tuning the electronic structures and surface properties, these strategies can boost the intrinsic activity of each active site, improve the number of active sites, and optimize the charge transfer process.

4. Concluding remarks and perspectives

In recent years, various metal oxide materials have been successfully fabricated as high-performance electrocatalysts for water splitting. In this review, different characterization techniques and fabrication strategies for HER and OER have been systematically summarized. We highlight that the abundance, diversity, and versatility of the transition metal oxides foresees a successful application in energy conversion devices. However, limited knowledge of the actual active sites in atomic scale during the electrochemistry still pose enormous challenges in further improvement in performance. We are in belief that metal oxide electrocatalysts will fulfil their potentials by addressing, at least if not all, the following fundamentally important barriers.

Firstly, although a variety of high-performance electrocatalysts have been developed, a mechanistic understanding of the surface charge transfer and catalytic sites during the electrochemical reaction is still highly demanding. Recently, some descriptors different from conventional ΔG_{H^*} and ($\Delta G_{O^*} - \Delta G_{HO^*}$) for HER and OER have been reported to evaluate the catalytic performance as well as rationally design materials. For example, the descriptor Φ considering the topological, bonding, and electronic structures of catalytic centre, the e_g-filling descriptor in perovskite oxides, and the one involved d band position are applied to predict the electrocatalytic activities towards HER and OER.[46,166,167] Additionally, advance in mechanistically understanding fundamental reaction steps has been realized by theoretical calculation, along with well-recognized principles providing useful avenues to study various electrochemistry towards other applications. However, mechanistic studies lack the understanding of reaction kinetics, which may need delicate experimental design. Therefore, combining with theoretical elucidations and experimental exploration, robust, high-performance electrocatalysts will be developed through effective catalyst activation strategies, such as single-atom or dual-atom sites creation, crystal phase engineering, heteroatoms doping, and interface manipulation.[168–171]

Secondly, the poor stability of the metal oxides electrocatalysts severely blocks their industrial application, compared with noble metal counterparts. Under long-term electrochemical test, the surface of metal oxides could undergo surface reconstruction, such as elemental enrichment or depletion.[172] Meanwhile, the dissolution or deposition of elec-

trode materials/impurities at the electrocatalyst/substrate interface may hamper the physical contact or restrict the reaction. For instance, Ru-based oxides are regarded as the most active OER materials, while they suffer from severe performance degradation due to Ru dissolution experimentally.[66] Therefore, improvement in structural robustness is essential to drive HER or OER for long-term operation. Moreover, in practical application, the current density required is usually higher than 1000 mA cm^{-2} for proton-exchange membrane (PEM) electrolyser, requiring catalysts with robust stability up to 1000 h.[173] To improve the long-term durability, incorporating molecular catalyst with carbon materials has been reported, significantly accelerating water oxidation half-reaction.[174] Although endowing with many advantages, the biggest challenge of PEM is that only noble metal-based materials can be used as working electrodes so far, wherein Pt-group metals (PGM) serve as cathode and Ir or Ru-based oxides as the anode. Recently, the development of alkaline anion exchange membrane (AEM) electrolysers provides possibility for the use of PGM-free catalysts, while the limited durability remains a challenge to be solved.[175] Over the last decade, alkaline membrane fuel cells (AMFCs) have been achieved with improved current densities and stability.[176] An AMFC operated continuously for over 1000 h at 600 mA cm^{-2} has been reported by developing gas diffusion electrodes (GDL) with hydrophobic PTFE in both the GDL and catalyst layers.[177] Thus, the structural integrity of the metal oxides should be assessed with a detailed investigation on the structural degradation or mechanical breakdown.[178]

Thirdly, accompanying with the development of theoretical methods, complementary *operando* characterization techniques are also highly desirable to precisely detect structures vibration and identify active sites during electrocatalysis process. Therefore, a rational design of well-defined electrochemically active components needs to comprehensively be tested with various parameters combining with *in situ* probing techniques for the metal oxides (as shown in Part 2). These technologies are also of paramount importance for understanding the reaction mechanism more profoundly. For example, accurate *in situ* detection of the atomic or electron structure could be realized by employing well-defined atomically thin electrode materials or adopting surface-sensitive probing techniques.[65,179] Additionally, reactant isotope labelling experiments that utilize the kinetic isotope effects are also useful to probe the forming mechanisms of intermediates as well as rate-limiting step.[180]

In summary, the future industrial application of robust metal oxides for energy conversion and storage demands comprehensive advancement from techniques, theories, characterizations, and devices. We believe with a great development of these key elements, impactful breakthroughs in real-world large-scale water electrolysis are becoming indispensable in the expectable future.

Conflicts of interest

There are no conflicts to declare.

Acknowledgements

The authors acknowledge the financial support from Australian Research Council (Discovery Project and Discovery Early Career Researcher Award).

References

1 J. A. Turner, *Science*, 2004, **305**, 972.
2 T. R. Cook, D. K. Dogutan, S. Y. Reece, Y. Surendranath, T. S. Teets and D. G. Nocera, *Chem. Rev.*, 2010, **110**, 6474.
3 J. K. Norskov and C. H. Christensen, *Science*, 2006, **312**, 1322.
4 V. R. Stamenkovic, D. Strmcnik, P. P. Lopes and N. M. Markovic, *Nat. Mater.*, 2016, **16**, 57.
5 W. Chen, X. Hou, X. Shi and H. Pan, *ACS Appl. Mater. Interfaces*, 2018, **10**, 35289.
6 M. P. Browne, C. Domínguez and P. E. Colavita, *Curr. Opin. Electrochem.*, 2017, **7**, 208.
7 G. Ming, D. Y. Wang, C. C. Chen, B. J. Hwang and H. Dai, *Nano Res.*, 2016, **9**, 28.
8 G. Zhao, K. Rui, S. X. Dou and W. Sun, *Adv. Funct. Mater.*, 2018, **28**, 180329.
9 Y. Zhu, Q. Lin, Y. Zhong, H. A. Tahini, Z. Shao and H. Wang, *Energy Environ. Sci.*, 2020, **12**, 3361.
10 W. T. Hong, M. Risch, K. A. Stoerzinger, A. Grimaud, J. Suntivich and Y. Shao-Horn, *Energy Environ. Sci.*, 2015, **8**, 1404.
11 M. Tahir, L. Pan, F. Idrees, X. Zhang, L. Wang, J. J. Zou and Z. L. Wang, *Nano Energy*, 2017, **37**, 136.
12 N. T. Suen, S. F. Hung, Q. Quan, N. Zhang, Y. J. Xu and H. M. Chen, *Chem. Soc. Rev.*, 2017, **46**, 337.
13 F. Song, L. Bai, A. Moysiadou, S. Lee, C. Hu, L. Liardet and X. Hu, *J. Am. Chem. Soc.*, 2018, **140**, 7748.
14 J. Song, C. Wei, Z. F. Huang, C. Liu, L. Zeng, X. Wang and Z. J. Xu, *Chem. Soc. Rev.*, 2020, **49**, 2196.
15 C. Hu, L. Zhang and J. Gong, *Energy Environ. Sci.*, 2019, **12**, 2620.
16 L. Li, P. Wang, Q. Shao and X. Huang, *Chem. Soc. Rev.*, 2020, **49**, 3072.
17 J. Wang, Y. Gao, H. Kong, J. Kim, S. Choi, F. Ciucci, Y. Hao, S. Yang, Z. Shao and J. Lim, *Chem. Soc. Rev.*, 2020, **49**, 9154.
18 C. Acar and I. Dincer, *Int. J. Hydrogen Energy*, 2014, **39**, 1.
19 X. Zou and Y. Zhang, *Chem. Soc. Rev.*, 2015, **44**, 5148.
20 P. C. Vesborg, B. Seger and I. Chorkendorff, *J. Phys. Chem. Lett.*, 2015, **6**, 951.
21 C. G. Morales-Guio, L. A. Stern and X. Hu, *Chem. Soc. Rev.*, 2014, **43**, 6555.
22 I. C. Man, H. Y. Su, F. Calle-Vallejo, H. A. Hansen, J. I. Martínez, N. G. Inoglu, J. Kitchin, T. F. Jaramillo, J. K. Nørskov and J. Rossmeisl, *ChemCatChem*, 2011, **3**, 1159.
23 F. Y. Chen, Z. Y. Wu, Z. Adler and H. Wang, *Joule*, 2021, **5**, 1.

24 T. Maiyalagan, K. A. Jarvis, S. Therese, P. J. Ferreira and A. Manthiram, *Nat. Commun.*, 2014, **5**, 3949.
25 J. K. Norskov, T. Bligaard, B. Hvolbaek, F. Abild-Pedersen, I. Chorkendorff and C. H. Christensen, *Chem. Soc. Rev.*, 2008, **37**, 2163.
26 J. K. Nørskov, T. Bligaard, A. Logadottir, J. R. Kitchin, J. G. Chen, S. Pandelov and U. Stimming, *J. Electrochem. Soc.*, 2005, **152**, J23.
27 J. Greeley, T. F. Jaramillo, J. Bonde, I. B. Chorkendorff and J. K. Norskov, *Nat. Mater.*, 2006, **5**, 909.
28 J. Staszak-Jirkovsky, C. D. Malliakas, P. P. Lopes, N. Danilovic, S. S. Kota, K. C. Chang, B. Genorio, D. Strmcnik, V. R. Stamenkovic, M. G. Kanatzidis and N. M. Markovic, *Nat. Mater.*, 2016, **15**, 197.
29 R. Subbaraman, D. Tripkovic, K. C. Chang, D. Strmcnik, A. P. Paulikas, P. Hirunsit, M. Chan, J. Greeley, V. Stamenkovic and N. M. Markovic, *Nat. Mater.*, 2012, **11**, 550.
30 R. Subbaraman, D. Tripkovic, D. Strmcnik, K. C. Chang, M. Uchimura, A. P. Paulikas, V. Stamenkovic and N. M. Markovic, *Science*, 2011, **334**, 1256.
31 C. Hu, L. Zhang and J. J. Gong, *Energy Environ. Sci.*, 2019, **12**, 2620.
32 C. Campos-Roldán, R. González-Huerta and N. Alonso-Vante, *Electrochim. Acta*, 2018, **283**, 1829.
33 D. Strmcnik, P. P. Lopes, B. Genorio, V. R. Stamenkovic and N. M. Markovic, *Nano Energy*, 2016, **29**, 29.
34 J. Rossmeisl, A. Logadottir and J. K. Nørskov, *Chem. Phys.*, 2005, **319**, 178.
35 Z. Shi, X. Wang, J. Ge, C. Liu and W. Xing, *Nanoscale*, 2020, **12**, 13249.
36 X. Rong, J. Parolin and A. M. Kolpak, *ACS Catal.*, 2016, **6**, 1153.
37 A. Grimaud, O. Diaz-Morales, B. Han, W. T. Hong, Y. L. Lee, L. Giordano, K. A. Stoerzinger, M. T. M. Koper and Y. Shao-Horn, *Nat. Chem.*, 2017, **9**, 457.
38 B. Hammer and J. K. Norskov, *Nature*, 1995, **376**, 238.
39 B. Hammer and J. K. Nørskov, *Adv. Catal.*, 2000, **45**, 71.
40 P. Rüetschi and P. Delahay, *J. Chem. Phys.*, 1955, **23**, 556.
41 S. Trasatti, *J. Electroanal. Chem. Interfacial Electrochem.*, 1980, **111**, 125.
42 Y. Matsumoto, H. Yoneyama and H. Tamura, *J. Electroanal. Chem. Interfacial Electrochem.*, 1977, **83**, 167.
43 Y. Matsumoto and E. Sato, *Mater. Chem. Phys.*, 1986, **14**, 397.
44 J. O. M. Bockris, *J. Electrochem. Soc.*, 1984, **131**, 290.
45 J. Suntivich, H. A. Gasteiger, N. Yabuuchi, H. Nakanishi, J. B. Goodenough and Y. Shao-Horn, *Nat. Chem.*, 2011, **3**, 546.
46 J. Suntivich, K. J. May, H. A. Gasteiger, J. B. Goodenough and Y. Shao-Horn, *Science*, 2011, **334**, 1383.
47 F. Calle-Vallejo, N. G. Inoglu, H.-Y. Su, J. I. Martínez, I. C. Man, M. T. M. Koper, J. R. Kitchin and J. Rossmeisl, *Chem. Sci.*, 2013, **4**, 1245.
48 Y. L. Lee, J. Kleis, J. Rossmeisl, Y. Shao-Horn and D. Morgan, *Energy Environ. Sci.*, 2011, **4**, 3966.
49 W. T. Hong, R. E. Welsch and Y. Shao-Horn, *J. Phys. Chem. C*, 2015, **120**, 78.
50 C. Wei, Z. Feng, G. G. Scherer, J. Barber, Y. Shao-Horn and Z. J. Xu, *Adv. Mater.*, 2017, **29**, 1606800.
51 Z. Qiu, C. W. Tai, G. A. Niklasson and T. Edvinsson, *Energy Environ. Sci.*, 2019, **12**, 572.
52 C. Xie, W. Chen, S. Du, D. Yan, Y. Zhang, J. Chen, B. Liu and S. Wang, *Nano Energy*, 2020, **71**, 104653.
53 B. S. Yeo and A. T. Bell, *J. Am. Chem. Soc.*, 2011, **133**, 5587.
54 B. J. Trześniewski, O. Diaz-Morales, D. A. Vermaas, A. Longo, W. Bras, M. T. Koper and W. A. Smith, *J. Am. Chem. Soc.*, 2015, **137**, 15112.
55 M. Steimecke, G. Seiffarth and M. Bron, *Anal. Chem.*, 2017, **89**, 10679.
56 C. N. Brodsky, R. G. Hadt, D. Hayes, B. J. Reinhart, N. Li, L. X. Chen and D. G. Nocera, *Proc. Natl. Acad. Sci. U. S. A.*, 2017, **114**, 3855.
57 A. Bergmann, E. Martinez-Moreno, D. Teschner, P. Chernev, M. Gliech, J. F. De Araújo, T. Reier, H. Dau and P. Strasser, *Nat. Commun.*, 2015, **6**, 8625.
58 D. Friebel, M. W. Louie, M. Bajdich, K. E. Sanwald, Y. Cai, A. M. Wise, M. Cheng, D. Sokaras, T. Weng, R. Alonso-Mori, R. C. Davis, J. R. Bargar, J. K. Nørskov, A. Nilsson and A. T. Bell, *J. Am. Chem. Soc.*, 2015, **137**, 1305.
59 Z. Yan, H. Sun, X. Chen, H. Liu, Y. Zhao, H. Li, W. Xie, F. Cheng and J. Chen, *Nat. Commun.*, 2018, **9**, 1.
60 A. Nenning, A. K. Opitz, C. Rameshan, R. Rameshan, R. Blume, M. Havecker, A. Knop-Gericke, G. Rupprechter, B. Klotzer and J. Fleig, *J. Phys. Chem. C*, 2016, **120**, 1461.
61 H. Ali-Löytty, M. W. Louie, M. R. Singh, L. Li, H. G. Sanchez Casalongue, H. Ogasawara, E. J. Crumlin, Z. Liu, A. T. Bell, A. Nilsson and D. Friebel, *J. Phys. Chem. C*, 2016, **120**, 2247.
62 H. G. Sanchez Casalongue, M. L. Ng, S. Kaya, D. Friebel, H. Ogasawara and A. Nilsson, *Angew. Chem., Int. Ed.*, 2014, **53**, 7169.
63 M. Görlin, J. Ferreira de Araújo, H. Schmies, D. Bernsmeier, S. Dresp, M. Gliech, Z. Jusys, P. Chernev, R. Kraehnert, H. Dau and P. Strasser, *J. Am. Chem. Soc.*, 2017, **139**, 2070.
64 T. Miura, S. Tsunekawa, S. Onishi, T. Ina, K. Wang, G. Watanbe, C. Hu, H. Kondoh, T. Kawai and M. Yoshida, *Phys. Chem. Chem. Phys.*, 2021, **23**, 23280.
65 J. Deng, M. R. Nellist, M. B. Stevens, C. Dette, Y. Wang and S. W. Boettcher, *Nano Lett.*, 2017, **17**, 6922.
66 E. A. Paoli, F. Masini, R. Frydendal, D. Deiana, C. Schlaup, M. Malizia, T. W. Hansen, S. Horch, I. E. Stephens and I. Chorkendorff, *Chem. Sci.*, 2015, **6**, 190.
67 K. Karthick, S. Anantharaj, P. E. Karthik, B. Subramanian and S. Kundu, *Inorg. Chem.*, 2017, **56**, 6734.
68 S. Anantharaj, S. R. Ede, K. Sakthikumar, K. Karthick, S. Mishra and S. Kundu, *ACS Catal.*, 2016, **6**, 8069.
69 S. Anantharaj, P. E. Karthik, B. Subramanian and S. Kundu, *ACS Catal.*, 2016, **6**, 4660.
70 J. K. Nørskov, J. Rossmeisl, A. Logadottir, L. Lindqvist, J. R. Kitchin, T. Bligaard and H. Jonsson, *J. Phys. Chem. B*, 2004, **108**, 17886.

71 C. Zhu, A. L. Wang, W. Xiao, D. Chao, X. Zhang, N. H. Tiep, S. Chen, J. Kang, X. Wang and J. Ding, *Adv. Mater.*, 2018, **30**, 1705516.
72 L. Li, P. Wang, Q. Shao and X. Huang, *Adv. Mater.*, 2021, 2004243.
73 H. Wang, H. W. Lee, Y. Deng, Z. Lu, P. C. Hsu, Y. Liu, D. Lin and Y. Cui, *Nat. Commun.*, 2015, **6**, 7261.
74 Z. Lu, H. Wang, D. Kong, K. Yan, P. C. Hsu, G. Zheng, H. Yao, Z. Liang, X. Sun and Y. Cui, *Nat. Commun.*, 2014, **5**, 4345.
75 S. Zhou, X. Miao, X. Zhao, C. Ma, Y. Qiu, Z. Hu, J. Zhao, L. Shi and J. Zeng, *Nat. Commun.*, 2016, **7**, 11510.
76 Y. Sun, S. Gao, F. Lei, J. Liu, L. Liang and Y. Xie, *Chem. Sci.*, 2014, **5**, 3976.
77 J. Huang, J. Chen, T. Yao, J. He, S. Jiang, Z. Sun, Q. Liu, W. Cheng, F. Hu, Y. Jiang, Z. Pan and S. Wei, *Angew. Chem., Int. Ed.*, 2015, **54**, 8722.
78 V. Viswanathan, K. L. Pickrahn, A. C. Luntz, S. F. Bent and J. K. Norskov, *Nano Lett.*, 2014, **14**, 5853.
79 Y. P. Zhu, T. Y. Ma, M. Jaroniec and S. Z. Qiao, *Angew. Chem., Int. Ed.*, 2017, **56**, 1324.
80 H. Wang, S. Zhuo, Y. Liang, X. Han and B. Zhang, *Angew. Chem., Int. Ed.*, 2016, **55**, 9055.
81 X. Gao, H. Zhang, Q. Li, X. Yu, Z. Hong, X. Zhang, C. Liang and Z. Lin, *Angew. Chem., Int. Ed.*, 2016, **55**, 6290.
82 C. Zhu, D. Wen, S. Leubner, M. Oschatz, W. Liu, M. Holzschuh, F. Simon, S. Kaskel and A. Eychmuller, *Chem. Commun.*, 2015, **51**, 7851.
83 Y. Wang, F. Silveri, M. K. Bayazit, Q. Ruan, Y. Li, J. Xie, C. R. A. Catlow and J. Tang, *Adv. Energy Mater.*, 2018, **8**, 1801084.
84 K. D. Gilroy, X. Yang, S. Xie, M. Zhao, D. Qin and Y. Xia, *Adv. Mater.*, 2018, **30**, e1706312.
85 Y. Li, Z. G. Yu, L. Wang, Y. Weng, C. S. Tang, X. Yin, K. Han, H. Wu, X. Yu, L. M. Wong, D. Wan, X. R. Wang, J. Chai, Y. W. Zhang, S. Wang, J. Wang, A. T. S. Wee, M. B. H. Breese, S. J. Pennycook, T. Venkatesan, S. Dong, J. M. Xue and J. Chen, *Nat. Commun.*, 2019, **10**, 3149.
86 F. Zhou, A. Izgorodin, R. K. Hocking, L. Spiccia and D. R. MacFarlane, *Adv. Energy Mater.*, 2012, **2**, 1013.
87 H. Y. Su, Y. Gorlin, I. C. Man, F. Calle-Vallejo, J. K. Norskov, T. F. Jaramillo and J. Rossmeisl, *Phys. Chem. Chem. Phys.*, 2012, **14**, 14010.
88 C. W. Tung, Y. Y. Hsu, Y. P. Shen, Y. Zheng, T. S. Chan, H. S. Sheu, Y. C. Cheng and H. M. Chen, *Nat. Commun.*, 2015, **6**, 8106.
89 J. G. Lee, J. Hwang, H. J. Hwang, O. S. Jeon, J. Jang, O. Kwon, Y. Lee, B. Han and Y. G. Shul, *J. Am. Chem. Soc.*, 2016, **138**, 3541.
90 L. Fang, Z. Jiang, H. Xu, L. Liu, Y. guan, X. Gu and Y. Wang, *J. Catal.*, 2018, **357**, 238.
91 X. Han, G. He, Y. He, J. Zhang, X. Zheng, L. Li, C. Zhong, W. Hu, Y. Deng and T. Ma, *Adv. Energy Mater.*, 2018, **10**, e1702222.
92 H. Wu, T. Yang, Y. Du, L. Shen and G. W. Ho, *Adv. Mater.*, 2018, **30**, e1804341.
93 Y. Tong, Y. Guo, P. Chen, H. Liu, M. Zhang, L. Zhang, W. Yan, W. Chu, C. Wu and Y. Xie, *Chem*, 2017, **3**, 812.
94 M. Gong, W. Zhou, M. C. Tsai, J. Zhou, M. Guan, M. C. Lin, B. Zhang, Y. Hu, D. Y. Wang, J. Yang, S. J. Pennycook, B. J. Hwang and H. Dai, *Nat. Commun.*, 2014, **5**, 4695.
95 M. Gong, W. Zhou, M. J. Kenney, R. Kapusta, S. Cowley, Y. Wu, B. Lu, M. C. Lin, D. Y. Wang, J. Yang, B. J. Hwang and H. Dai, *Angew. Chem., Int. Ed.*, 2015, **54**, 11989.
96 H. Jin, J. Wang, D. Su, Z. Wei, Z. Pang and Y. Wang, *J. Am. Chem. Soc.*, 2015, **137**, 2688.
97 Y. Kuang, G. Feng, P. Li, Y. Bi, Y. Li and X. Sun, *Angew. Chem., Int. Ed.*, 2016, **55**, 693.
98 Z. Weng, W. Liu, L. C. Yin, R. Fang, M. Li, E. I. Altman, Q. Fan, F. Li, H. M. Cheng and H. Wang, *Nano Lett.*, 2015, **15**, 7704.
99 X. Yan, L. Tian, M. He and X. Chen, *Nano Lett.*, 2015, **15**, 6015.
100 M. R. Gao, Y. F. Xu, J. Jiang, Y. R. Zheng and S. H. Yu, *J. Am. Chem. Soc.*, 2012, **134**, 2930.
101 K. Li, J. Zhang, R. Wu, Y. Yu and B. Zhang, *Adv. Sci.*, 2016, **3**, 1500426.
102 C. Hu, L. Zhang, Z. J. Zhao, J. Luo, J. Shi, Z. Huang and J. Gong, *Adv. Mater.*, 2017, **29**, 1701820.
103 H. Hu, B. Guan, B. Xia and X. W. Lou, *J. Am. Chem. Soc.*, 2015, **137**, 5590.
104 M. Tahir, L. Pan, R. Zhang, Y. C. Wang, G. Shen, I. Aslam, M. A. Qadeer, N. Mahmood, W. Xu, L. Wang, X. Zhang and J. J. Zou, *ACS Energy Lett.*, 2017, **2**, 2177.
105 J. X. Feng, S. H. Ye, H. Xu, Y. X. Tong and G. R. Li, *Adv. Mater.*, 2016, **28**, 4698.
106 Y. R. Zheng, M. R. Gao, Q. Gao, H. H. Li, J. Xu, Z. Y. Wu and S. H. Yu, *Small*, 2015, **11**, 182.
107 X. Long, H. Lin, D. Zhou, Y. An and S. Yang, *ACS Energy Lett.*, 2018, **3**, 290.
108 Y. Zhao, X. Jia, G. Chen, L. Shang, G. I. Waterhouse, L. Z. Wu, C. H. Tung, D. O'Hare and T. Zhang, *J. Am. Chem. Soc.*, 2016, **138**, 6517.
109 L. C. Seitz, C. F. Dickens, K. Nishio, Y. Hikita, J. Montoya, A. Doyle, C. Kirk, A. Vojvodic, H. Y. Hwang, J. K. Norskov and T. F. Jaramillo, *Science*, 2016, **353**, 1011.
110 H. Li, Q. Zhou, F. Liu, W. Zhang, Z. Tan, H. Zhou, Z. Huang, S. Jiao and Y. Kuang, *Appl. Catal., B*, 2019, **255**, 117755.
111 X. Xu, Y. Chen, W. Zhou, Z. Zhu, C. Su, M. Liu and Z. Shao, *Adv. Mater.*, 2016, **28**, 6442.
112 T. Ling, T. Zhang, B. Ge, L. Han, L. Zheng, F. Lin, Z. Xu, W. B. Hu, X. W. Du, K. Davey and S. Z. Qiao, *Adv. Mater.*, 2019, **31**, e1807771.
113 X. Zhong, Y. Sun, X. Chen, G. Zhuang, X. Li and J. G. Wang, *Adv. Funct. Mater.*, 2016, **26**, 5778.
114 M. Retuerto, L. Pascual, F. Calle-Vallejo, P. Ferrer, D. Gianolio, A. G. Pereira, A. Garcia, J. Torrero, M. T. Fernandez-Diaz, P. Bencok, M. A. Pena, J. L. G. Fierro and S. Rojas, *Nat. Commun.*, 2019, **10**, 2041.

115 J. T. Mefford, X. Rong, A. M. Abakumov, W. G. Hardin, S. Dai, A. M. Kolpak, K. P. Johnston and K. J. Stevenson, *Nat. Commun.*, 2016, **7**, 11053.
116 Y. Zhu, W. Zhou, Y. Chen, J. Yu, M. Liu and Z. Shao, *Adv. Mater.*, 2015, **27**, 7150.
117 B. Weng, F. Xu, C. Wang, W. Meng, C. R. Grice and Y. Yan, *Energy Environ. Sci.*, 2017, **10**, 121.
118 X. Liu, Z. Chang, L. Luo, T. Xu, X. Lei, J. Liu and X. Sun, *Chem. Mater.*, 2014, **26**, 1889.
119 X. Xu, C. Su, W. Zhou, Y. Zhu, Y. Chen and Z. Shao, *Adv. Sci.*, 2016, **3**, 1500187.
120 K. Fominykh, P. Chernev, I. Zaharieva, J. Sicklinger, G. Stefanic, M. Doblinger, A. Muller, A. Pokharel, S. Bocklein, C. Scheu, T. Bein and D. Fattakhova-Rohlfing, *ACS Nano*, 2015, **9**, 5180.
121 M. K. Bates, Q. Jia, H. Doan, W. Liang and S. Mukerjee, *ACS Catal.*, 2015, **6**, 155.
122 N. Li, D. K. Bediako, R. G. Hadt, D. Hayes, T. J. Kempa, F. von Cube, D. C. Bell, L. X. Chen and D. G. Nocera, *Proc. Natl. Acad. Sci. U. S. A.*, 2017, **114**, 1486.
123 Y. Liu, Y. Ying, L. Fei, Y. Liu, Q. Hu, G. Zhang, S. Y. Pang, W. Lu, C. L. Mak, X. Luo, L. Zhou, M. Deng and H. Huang, *J. Am. Chem. Soc.*, 2019, **141**, 8136.
124 Y. Zhu, W. Zhou, Z. G. Chen, Y. Chen, C. Su, M. O. Tadé and Z. Shao, *Angew. Chem.*, 2015, **127**, 3969.
125 S. Yagi, I. Yamada, H. Tsukasaki, A. Seno, M. Murakami, H. Fujii, H. Chen, N. Umezawa, H. Abe, N. Nishiyama and S. Mori, *Nat. Commun.*, 2015, **6**, 8249.
126 Y. Duan, S. Sun, S. Xi, X. Ren, Y. Zhou, G. Zhang, H. Yang, Y. Du and Z. J. Xu, *Chem. Mater.*, 2017, **29**, 10534.
127 N. Zhang, C. Wang, J. Chen, C. Hu, J. Ma, X. Deng, B. Qiu, L. Cai, Y. Xiong and Y. Chai, *ACS Nano*, 2021, **15**, 8537.
128 N. B. Halck, V. Petrykin, P. Krtil and J. Rossmeisl, *Phys. Chem. Chem. Phys.*, 2014, **16**, 13682.
129 Z. Xiao, Y. Wang, Y. C. Huang, Z. Wei, C. L. Dong, J. Ma, S. Shen, Y. Li and S. Wang, *Energy Environ. Sci.*, 2017, **10**, 2563.
130 K. Liu, W. Zhang, F. Lei, L. Liang, B. Gu, Y. Sun, B. Ye, W. Ni and Y. Xie, *Nano Energy*, 2016, **30**, 810.
131 Y. Zhu, W. Zhou, J. Sunarso, Y. Zhong and Z. Shao, *Adv. Funct. Mater.*, 2016, **26**, 5862.
132 X. Li, J. Wei, Q. Li, S. Zheng, Y. Xu, P. Du, C. Chen, J. Zhao, H. Xue and Q. Xu, *Adv. Funct. Mater.*, 2018, **28**, 1800886.
133 J. Fu, F. M. Hassan, C. Zhong, J. Lu, H. Liu, A. Yu and Z. Chen, *Adv. Mater.*, 2017, **29**, 1702526.
134 S. Dou, C. L. Dong, Z. Hu, Y. C. Huang, J. l. Chen, L. Tao, D. Yan, D. Chen, S. Shen, S. Chou and S. Wang, *Adv. Funct. Mater.*, 2017, **27**, 1702546.
135 Y. Kwon, T. Y. Kim, G. Kwon, J. Yi and H. Lee, *J. Am. Chem. Soc.*, 2017, **139**, 17694.
136 J. C. Liu, Y. G. Wang and J. Li, *J. Am. Chem. Soc.*, 2017, **139**, 6190.
137 S. Nong, W. Dong, J. Yin, B. Dong, Y. Lu, X. Yuan, X. Wang, K. Bu, M. Chen, S. Jiang, L. M. Liu, M. Sui and F. Huang, *J. Am. Chem. Soc.*, 2018, **140**, 5719.
138 F. Cheng, J. Shen, B. Peng, Y. Pan, Z. Tao and J. Chen, *Nat. Chem.*, 2011, **3**, 79.
139 J. Hong, Z. Hu, M. Probert, K. Li, D. Lv, X. Yang, L. Gu, N. Mao, Q. Feng, L. Xie, J. Zhang, D. Wu, Z. Zhang, C. Jin, W. Ji, X. Zhang, J. Yuan and Z. Zhang, *Nat. Commun.*, 2015, **6**, 6293.
140 Y. Liu, H. Cheng, M. Lyu, S. Fan, Q. Liu, W. Zhang, Y. Zhi, C. Wang, C. Xiao, S. Wei, B. Ye and Y. Xie, *J. Am. Chem. Soc.*, 2014, **136**, 15670.
141 R. Zhang, Y. C. Zhang, L. Pan, G. Q. Shen, N. Mahmood, Y. H. Ma, Y. Shi, W. Jia, L. Wang, X. Zhang, W. Xu and J. J. Zou, *ACS Catal.*, 2018, **8**, 3803.
142 D. Chen, M. Qiao, Y. R. Lu, L. Hao, D. Liu, C. L. Dong, Y. Li and S. Wang, *Angew. Chem., Int. Ed.*, 2018, **57**, 8691.
143 Y. H. Li, P. F. Liu, L. F. Pan, H. F. Wang, Z. Z. Yang, L. R. Zheng, P. Hu, H. J. Zhao, L. Gu and H. G. Yang, *Nat. Commun.*, 2015, **6**, 8064.
144 T. Ling, D. Y. Yan, Y. Jiao, H. Wang, Y. Zheng, X. Zheng, J. Mao, X. W. Du, Z. Hu, M. Jaroniec and S. Z. Qiao, *Nat. Commun.*, 2016, **7**, 12876.
145 Q. Feng, S. Zhao, D. He, S. Tian, L. Gu, X. Wen, C. Chen, Q. Peng, D. Wang and Y. Li, *J. Am. Chem. Soc.*, 2018, **140**, 2773.
146 T. Ling, D. Y. Yan, H. Wang, Y. Jiao, Z. Hu, Y. Zheng, L. Zheng, J. Mao, H. Liu, X. W. Du, M. Jaroniec and S. Z. Qiao, *Nat. Commun.*, 2017, **8**, 1509.
147 J. R. Petrie, H. Jeen, S. C. Barron, T. L. Meyer and H. N. Lee, *J. Am. Chem. Soc.*, 2016, **138**, 7252.
148 J. Hwang, Z. Feng, N. Charles, X. R. Wang, D. Lee, K. A. Stoerzinger, S. Muy, R. R. Rao, D. Lee, R. Jacobs, D. Morgan and Y. Shao-Horn, *Mater. Today*, 2019, **31**, 100.
149 Y. Zang, S. Niu, Y. Wu, X. Zheng, J. Cai, J. Ye, Y. Xie, Y. Liu, J. Zhou, J. Zhu, X. Liu, G. Wang and Y. Qian, *Nat. Commun.*, 2019, **10**, 1217.
150 J. R. Petrie, V. R. Cooper, J. W. Freeland, T. L. Meyer, Z. Zhang, D. A. Lutterman and H. N. Lee, *J. Am. Chem. Soc.*, 2016, **138**, 2488.
151 R. D. L. Smith, B. Sporinova, R. D. Fagan, S. Trudel and C. P. Berlinguette, *Chem. Mater.*, 2014, **26**, 1654.
152 H. Vrubel, D. Merki and X. Hu, *Energy Environ. Sci.*, 2012, **5**, 6136.
153 D. Gonzalez-Flores, I. Sanchez, I. Zaharieva, K. Klingan, J. Heidkamp, P. Chernev, P. W. Menezes, M. Driess, H. Dau and M. L. Montero, *Angew. Chem., Int. Ed.*, 2015, **54**, 2472.
154 A. Indra, P. W. Menezes, N. R. Sahraie, A. Bergmann, C. Das, M. Tallarida, D. Schmeisser, P. Strasser and M. Driess, *J. Am. Chem. Soc.*, 2014, **136**, 17530.
155 L. Kuai, J. Geng, C. Chen, E. Kan, Y. Liu, Q. Wang and B. Geng, *Angew. Chem., Int. Ed.*, 2014, **53**, 7547.
156 T. Gao, Z. Jin, M. Liao, J. Xiao, H. Yuan and D. Xiao, *J. Mater. Chem. A*, 2015, **3**, 17763.
157 Y. Zhang, T. Gao, Z. Jin, X. Chen and D. Xiao, *J. Mater. Chem. A*, 2016, **4**, 15888.
158 Y. R. Hong, S. Mhin, K.-M. Kim, W.-S. Han, H. Choi, G. Ali, K. Y. Chung, H. J. Lee, S.-I. Moon, S. Dutta, S. Sun,

Y.-G. Jung, T. Song and H. Han, *J. Mater. Chem. A*, 2019, **7**, 3592.
159 Z. Zhu, H. Yin, C. He, M. Al-Mamun, P. Liu, L. Jiang, Y. Zhao, Y. Wang, H. Yang, Z. Tang, D. Wang, X. Chen and H. Zhao, *Adv. Mater.*, 2018, **30**, 1801171.
160 J. Roy, M. Al-Mamun, H. Yin, Y. Dou, L. Zhang, P. Liu, Y. Wang, Y. Zhong and H. Zhao, *ChemPlusChem*, 2020, **85**, 1602.
161 Y. Dou, C. He, L. Zhang, H. Yin, M. Al-Mamun, J. Ma and H. Zhao, *Nat. Commun.*, 2020, **11**, 1664.
162 S. Jin, *ACS Energy Lett.*, 2017, **2**, 1937.
163 L. Stern, L. Feng, F. Song and X. H, *Energy Environ. Sci.*, 2015, **8**, 2347.
164 X. Xu, F. Song and X. Hu, *Nat. Commun.*, 2016, **7**, 12324.
165 W. Chen, H. Wang, Y. Li, Y. Liu, J. Sun, S. Lee, J. Lee and Y. Cui, *ACS Cent. Sci.*, 2015, **1**, 244.
166 L. Gong, D. Zhang, C. Y. Lin, Y. Zhu, Y. Shen, J. Zhang, X. Han, L. Zhang and Z. Xia, *Adv. Energy Mater.*, 2019, **9**, 1902625.
167 C. Wei, Y. Sun, G. G. Scherer, A. C. Fisher, M. P. Sherburne, J. W. Ager, Z. J. Xu and J. Am, *Chem. Soc.*, 2020, **142**, 7765.
168 J. Wan, Z. Zhao, H. Shang, B. Peng, W. Chen, J. Pei, L. Zheng, J. Dong, R. Cao, R. Sarangi, Z. Jiang, D. Zhou, Z. Zhuang, J. Zhang, D. Wang and Y. Li, *J. Am. Chem. Soc.*, 2020, **142**, 8431.
169 Z. Jiang, W. Zhou, A. Hong, M. Guo, X. Luo and C. Yuan, *ACS Energy Lett.*, 2019, **4**, 2830.
170 Y. Pan, X. Xu, Y. Zhong, L. Ge, Y. Chen, J. P. M. Veder, D. Guan, R. O'Hayre, M. Li, G. Wang, H. Wang, W. Zhou and Z. Shao, *Nat. Commun.*, 2020, **11**, 2002.
171 J. Li, D. Chu, H. Dong, D. R. Baker and R. Jiang, *J. Am. Chem. Soc.*, 2019, **10**, 269.
172 J. T. S. Irvine, D. Neagu, M. C. Verbraeken, C. Chatzichristodoulou, C. Graves and M. B. Mogensen, *Nat. Energy*, 2016, **1**, 15014.
173 Y. Luo, L. Tang, U. Khan, Q. Yu, H.-M. Cheng, X. Zou and B. Liu, *Nat. Commun.*, 2020, **11**, 2002.
174 B. Zhang, L. Fan, R. B. Ambre, T. Liu, Q. Meng, B. J. J. Timmer and L. Sun, *Joule*, 2020, **4**, 1408.
175 D. Li, E. J. Park, W. Zhu, Q. Shi, Y. Zhou, H. Tian, Y. Lin, A. Serov, B. Zulevi, E. D. Baca, C. Fujimoto, H. T. Chung and Y. S. Kim, *Nat. Energy*, 2020, **5**, 378.
176 S. J. C. Cleghorn, D. K. Mayfield, D. A. Moore, J. C. Moore, G. Rusch, T. W. Sherman, N. T. Sisofo and U. Beuscher, *J. Power Sources*, 2006, **158**, 446.
177 X. Peng, D. Kulkarni, Y. Huang, T. J. Omasta, B. Ng, Y. Zheng, L. Wang, J. M. LaManna, D. S. Hussey, J. R. Varcoe, I. V. Zenyuk and W. E. Mustain, *Nat. Commun.*, 2020, **11**, 3561.
178 K. J. May, C. E. Carlton, K. A. Stoerzinger, M. Risch, J. Suntivich, Y.-L. Lee, A. Grimaud and Y. Shao-Horn, *J. Phys. Chem. Lett.*, 2012, **3**, 3264.
179 Y. R. Shen, *Nature*, 1989, **337**, 519.
180 S. Haschke, M. Mader, S. Schlicht, A. M. Roberts, A. M. Angeles-Boza, J. A. C. Barth and J. Bachmann, *Nat. Commun.*, 2018, **9**, 4565.